Unjamming overcomes kinetic and proliferation arrest in terminally differentiated cells and promotes collective motility of carcinoma

Andrea Palamidessi[1#], Chiara Malinverno[1,2,#,*], Emanuela Frittoli[1#], Salvatore Corallino[1], Elisa Barbieri[3], Sara Sigismund[2,3], Galina V. Beznoussenko[1], Emanuele Martini[1], Massimiliano Garre'[1], Ines Ferrara[4], Claudio Tripodo[1,4], Flora Ascione[1], Elisabetta A. Cavalcanti-Adam[6], Qingsen Li [1], Pier Paolo Di Fiore[2,3], Dario Parazzoli[1], Fabio Giavazzi[5 *], Roberto Cerbino[5 *], Giorgio Scita[1,2 *].

[1]IFOM, the FIRC Institute of Molecular Oncology, Via Adamello 16, 20139, Milan, Italy
[2]University of Milan, Department of Oncology and Hemato-Oncology, Via Santa Sofia 9/1, 20122 Milan, Italy
[3]Istituto Europeo di Oncologia IRCCS, Via Ripamonti 435, 20141, Milan, Italy
[4]Department of Health Sciences, Human Pathology Section, University of Palermo School of Medicine Via del Vespro 129, 90127, Palermo, Italy
[5]University of Milan, Department of Medical Biotechnology and Translational Medicine, Via F.lli Cervi 93, 20090 Segrate, Italy
[6]Max Planck Institute for Medical Research, Heidelberg, Germany

[#] These authors contributed equally to this work.

[*]These authors are all equally responsible for this work.

Correspondence to: Giorgio.Scita@ifom.eu (ORCID- 0000-0001-7984-1889)
or Chiara.Malinverno@ifom.eu (ORCID-0000-0002-9470-8805) or roberto.cerbino@unimi.it (ORCID-0000-0003-0434-7741) or Fabio.giavazzi@unimi.it (ORCID-0000-0003-4930-0592)

Abstract (145-words)

During wound repair, branching morphogenesis and carcinoma dissemination, cellular rearrangements are fostered by a solid-to-liquid transition, known as unjamming. The biomolecular machinery behind unjamming and its pathophysiological relevance remain, however, unclear. Here, we study unjamming in a variety of normal and tumorigenic epithelial 2D and 3D collectives. Biologically, the increased level of the small GTPase RAB5A sparks unjamming by promoting non-clathrin-dependent internalization of epidermal growth factor receptor that leads to hyper-activation of the kinase ERK1/2 and phosphorylation of the actin nucleator WAVE2. This cascade triggers collective motility effects with striking biophysical consequences. Specifically, unjamming in tumor spheroids is accompanied by persistent and coordinated rotations that progressively remodel the extracellular matrix, while simultaneously fluidizing cells at the periphery. This concurrent action results in collective invasion, supporting the concept that the endo-ERK1/2 pathway is a physicochemical switch to initiate collective invasion and dissemination of otherwise jammed carcinoma.

Collective motility is ruled by both biochemical and physical interactions that cells establish among each other and with their environment[1, 2]. During tissue growth cells are free to move, as in a fluid, but their motion becomes constrained as density increases. At a critical density - depending on a variety of biophysical parameters, such as intercellular adhesion, cortical tension, single cell motility, and cell shape variance, motility ceases and collectives rigidify undergoing jamming transition[3-7]. This transition ensures proper development of barrier properties in epithelial tissues, but also to act as a tumour suppressive mechanism[3, 8]. The reverse solid-to-liquid (unjamming) transition might, instead, represent a complementary gateway to epithelial cell migration, enabling mature tissues to flow[3, 8, 9]. However, how cells control the jamming/unjamming transition is unclear.

Consistently with the emerging role of membrane trafficking in regulating cell migration plasticity and the mechanics of cell-cell interactions[10, 11], we recently found that RAB5A, a master regulator of early endosomes necessary to promote a mesenchymal program of individual cancer invasion[12, 13], impacts on the mechanics and dynamics of multicellular, normal and tumorigenic cell assemblies[14]. RAB5A overexpression re-awakens the motility of otherwise kinetically-arrested epithelial monolayers, promoting millimetre-scale, multicellular, ballistic cell locomotion and a flocking-fluid motility pattern through large-scale coordinated migration and local cell rearrangements[14-16]. Concurrently, monolayer stiffness, cell-cell surface contact and junctional tension increase, as well as the turnover of junctional E-cadherin and the extension of RAC1-driven protrusions[14]. Molecularly, impairing endocytosis, macropinocytosis or increasing fluid efflux abrogated RAB5A-induced collective motility, suggesting that perturbations of trafficking processes are necessary for the unjamming transition. However, the molecular nature of these endocytic-sensitive pathways is yet unidentified. Even less clear is whether this transition occurs in relevant physiological, three-dimensional settings and whether it can promote collective dissemination of dense, jammed carcinoma.

Here, we identify a necessary axis of the flocking transition in a variety of jammed collectives.

RAB5A overexpression enhances the internalization of the epidermal growth factor receptor (EGFR) through non-clathrin-dependent routes into endosomes, which causes hyper-activation of the extracellular signal-regulated protein kinases ERK1/2 and the phosphorylation of the branched actin nucleator, WAVE2[17]. This endocytic-ERK1/2 axis is sufficient to overcome the kinetic and proliferation arrest of mammary cysts in 3D. It also stimulates coherent rotation of breast ductal carcinoma in situ (DCIS) spheroid models, which causes both a radial gradient of cell fluidification and a stress-induced remodelling of the surrounding extracellular matrix. These effects combine to promote collective invasion of DCIS spheroids and *ex vivo* slices of orthotopically-implanted DCIS, pointing at the identified RAB5A-mediated, epidermal growth factor (EGF)-dependent activation of endosomal ERK1/2 as a key molecular route to the unjamming-via-flocking transition**.** Pathologically, the identified pathway appears relevant for breast carcinoma, RAB5A expression being upregulated in invasive foci of human DCIS and correlating with worse disease-free survival.

Results

EGFR trafficking controls flocking-liquid motility

RAB5A expression promotes a flocking transition in jammed/solid epithelial monolayers[14] through ill-defined molecular mechanisms and signalling axes. Particle Image Velocimetry (PIV) revealed that RAB5A expression enhanced cell motility, quantified by the root mean square velocity v_{RMS} (see Methods). It further promoted millimetres-scale coordination, measured by the velocity correlation length L_{corr}, and directed collective motion over a distance larger than ~700 μm, quantified by the persistence length L_{pers}, confirming previous results[14]. Removal of EGF, required for proliferation and single cell motility of MCF10A[18], or addition of AG1478, an inhibitor of the EGFR kinase[19], abrogated RAB5A-induced flocking (Supplementary Supplementary Movies 1, 2 and 4), with v_{RMS}, L_{corr}, and L_{pers} reverting to values typical of control cells (Figure 1A). These treatments further impacted on the uniformity of the migration pattern (Figure 1B). We confirmed these results using EGFP-H2B-expressing cells to visualize nuclear cell displacements (Supplementary Movie 3). Finally, similar EGF-dependency of collective motion was also observed in serum-starved, jammed keratinocyte monolayers, HaCat[20], and in oncogenically-transformed MCF10A variants, MCF10.DCIS.com (Supplementary Figure 8A and - Supplementary Movie 20).

Next, we tested whether alterations of endosomal biogenesis caused by RAB5A[21] perturb EGFR cellular distribution, trafficking or signalling. Firstly, we showed that the total protein, but not the mRNA levels of EGFR were significantly reduced following induction of RAB5A expression (Figure 1C-D). The fraction of phosphorylated EGFR was, instead, unexpectedly increased (Figure 1C). Secondly, RAB5A-expressing cells display a marked reduction of cell surface EGFR accompanied by increased intracellular EGFR, which accumulates in EEA1-positive, early endosomes (Figure 1E-G). Measurements of the absolute number of surface EGFR using ^{125}I-EGF binding corroborated the immunofluorescence (IF) data (Figure 1H). Finally, by IF analysis (Supplementary Figure 1A-C, Supplementary Table 1) and by determining the number of EGFR molecules on the plasma membrane

(PM) (Supplementary Figure 1D), we verified that the removal of the ligand and inhibition of EGFR kinase activity restore EGFR surface and intracellular distribution to levels of control cells.

Intracellular accumulation of EGFR might originate from increased internalization or reduced recycling. In the former case, In the former case, it is known that for a low EGF dose (1 ng/ml), EGFRs are primarily internalized by Clathrin-mediated endocytosis[22] and recycled back to the PM[23]. For large physiological EGF concentrations (20-to-100 ng/ml), non-Clathrin endocytosis[24] is activated in parallel to Clathrin-mediated endocytosis[23, 25]. RAB5A expression significantly increased the apparent endocytic rate constant (Ke) at high (30 ng/ml), but not at low (1 ng/ml) ^{125}I-EGF concentrations (Figure 2A). We also measured recycling rates of EGFR, which were not significantly altered by elevation of RAB5A (Figure 2B), and the total levels of EGFR, which were slowly, but progressively decreased over time consistent with the augmented non-clathrin internalization that target EGFR to degradation (Supplementary Figure 1E). To reinforce this finding, we measured EGFR internalization at high doses of ligands after silencing critical determinants of Clathrin- and non-Clathrin-endocytosis. We found that silencing Dynamin-2 robustly reduced EGFR internalization by more than 80% in both control and RAB5A cells, consistent with the expected requirement of this protein for EGFR entry (Figure 2C-D, Supplementary Table 2). The silencing of Clathrin inhibited EGFR internalization to an extent similar to the one achieved by Dynamin-2 siRNA in control cells, but was significantly less effective in RAB5A-expressing cells (Figure 2C-D, Supplementary Table 2). Finally, the RAB5A-dependent increased rate of endocytosis was reduced to control levels after silencing of the ER resident protein Reticulon 3 (RTN3), essential for non-Clathrin endocytosis[25] (Figure 2C), or by impairing macropinocytosis using 5-(N-ethyl-Nisopropyl) amiloride, EIPA[26] (Figure 2E). Collectively, these findings indicate that RAB5A promotes EGFR non-Clathrin endocytosis, leading to accumulation of EGFR into early endosomes and, possibly, to the re-awakening of collective motion. Indeed, silencing of Dynamin-2 (Supplementary Figure 2A-

B, Supplementary Movie 5), or RTN3, but not of its highly-related ER resident protein RTN4 (Supplementary Figure 2C-D, Supplementary Movie 6), impaired RAB5A-induced flocking.

RAB5A activates ERK1/2 to regulate cell protrusions dynamics

EGFR signalling has been proposed to be initiated at the plasma membrane but to continue in endosomes[27-29], which act as signalling quanta-like platforms where phosphorylated EGFR can be packaged at constant mean amounts[30]. As a consequence, altering the size and number of endosomes directly affected EGFR signalling. Hence, we monitored EGFR downstream pathways following RAB5A expression.

We found no impact on phosphorylation levels of the two kinases AKT and p38, variably involved in motility, whereas phosphorylated ERK1/2 was increased (Figure 3A) and long-lived in RAB5A-expressing cells (Supplementary Figure 3A, Supplementary Table 3). We corroborated this finding by IF after mixing control and EGFP-H2B-RAB5A-expressing cells (Supplementary Figure 3B). Notably, ERK1/2 activation was detectable only in RAB5A, but not in RAB5B- or RAB5C-expressing cells (Supplementary Figure 3C-D). Only RAB5A increased significantly both the number and size distribution of EEA1-positive endosomes (Supplementary Figure 3E-H, Supplementary Table 4), and significantly reduced surface EGFR levels, while augmenting the number of EGFR+ structures (Supplementary Figure 4A-E). RAB5B, instead, had marginal effects on endosome size and number, whereas RAB5C decreased significantly endosome number but robustly increased the size of EEA1- and EGFR-positive endosomes, which were concentrated perinuclearly (Supplementary Figures 3E-H and 4A-E). RAB5B and RAB5C were also very inefficient in reawakening collective motion in jammed monolayers (Supplementary Figure 4F, Supplementary Movie 7). Additionally, pharmacological inhibition of ERK1/2 using PD0325901 that targets the upstream MEK kinase[31], or SCH772984 that directly inhibits ERK1/2 activity, abrogated RAB5A-induced flocking (Figure 3B, Supplementary Movie 8). Treatment with AG1478 or Dynasore, a small

molecule impairing Dynamin-2 activity[32], inhibited RAB5A-mediated elevation of ERK1/2 (Figure 3C) and blocked the reawakening of collective motion (Figure 1, Supplementary Movies 2, 9 and ref[14]), suggesting that RAB5A elevation might enhance endosomal ERK1/2 signalling. This conjecture was tested by generating a FRET EKAREV-ERK1/2 sensor[33], targeted to the endosomes by appending the FYVE domain of SARA protein to its C-terminus[34] (Supplementary Figure 4G-H). Removal of EGF or treatment with PD0325901 significantly impaired FRET efficiency validating the biological relevance of the sensor (Supplementary Figure 4I). More importantly, RAB5A-expressing cells displayed increased endosomal ERK1/2 FRET efficiency as compared to control monolayers (Supplementary Figure 4J). We further showed that global elevation of ERK1/2 phosphorylation induced by the expression of a constitutively activated MEK-DD did not reawaken motility in jammed monolayers (Supplementary Figure 5A-B, Supplementary Movie 10). Notably, MEK-DD had no impact of junctional straightness or morphology (Supplementary Figure 5C-D). Collectively, our findings indicate that ERK1/2 activation is necessary, albeit not sufficient, to promote unjamming.

RAB5A-expressing, unjammed monolayers move in a directed fashion by extending oriented cryptic lamellipodia (Figure 3D and Ref[14, 35]). Cryptic lamellipodia depend on RAC1, which activates branched actin polymerization of the pentameric WAVE2 complex[36]. The key component of this complex, WAVE2 is phosphorylated by ERK1/2 on multiple serine residues, among which S343 and S351, to be activated and to control protrusion dynamics[37]. Consistently, we found that RAB5A expression increased the phosphorylation of WAVE2, but marginally of ABI1, another key component of the WAVE complex[36], in an ERK1/2, EGFR and Dynamin-2-dependent manner (Supplementary Figure 6A-C). Additionally, by monitoring the dynamics of cells mosaically-expressing EGFP-LifeAct, we found that pharmacological inhibition of ERK1/2 impaired the formation and dynamics of cryptic lamellipodia (Figure 3D-E, Supplementary Movie 11). Similar results were obtained by silencing of NAP1, a critical member of the complex. This treatment

185 destabilized both WAVE2 and ABI1 proteins (Figure 3F), as previously shown[38, 39], impaired cryptic
186 lamellipodia dynamics (Figure 3G, Supplementary Movie 12), flocking (Figure 3H, Supplementary
187 Movie 13), and wound closure (Supplementary Figure 6D-F, Supplementary Movie 14). Silencing of
188 the sole WAVE2 in MCF10A cells, which express also WAVE1 and WAVE3 mRNA
189 (Supplementary Figure 6G), was, as expected, less effective (Supplementary Figure 6D-E,
190 Supplementary Movie 14).
191
192 **Unjamming terminally-differentiated mammary acini**
193 To explore the biological consequence of RAB5A-induced endo-ERK1/2 axis, we exploited the
194 ability of MCF10A cells to generate differentiated, kinetically and proliferation-arrested hollow cysts
195 grown over Matrigel plugs (Supplementary Figure 7A and ref[18]). We employed mCherry-H2B-
196 expressing control and RAB5A-cells to monitor the kinematics of differentiated cysts (Figure 4A).
197 Cells in control differentiated acini were kinetically-arrested, whereas expression of RAB5A
198 reawakened motility by triggering rotational motion (Figure 4B-C, Supplementary Movie 15). With
199 custom PIV, we quantified the tangential rotational velocity field and extracted relevant kinematic
200 parameters, such as the root mean square velocity v_{RMS} and the rotational order parameter ψ, which
201 can vary between 0 (absence of coordinated motion) and 1 (for a rigidly rotating sphere) (see
202 Methods). Control acini displayed barely detectable v_{RMS}, with ψ below 0.2 (Figure 4C,
203 Supplementary Movies 15-16), whereas following RAB5A-expression ψ reached a value close to 1
204 in correspondence of the maximum of v_{RMS} (Figure 4C, Supplementary Movies 15-16).
205 Impairing EGFR activity, ERK1/2 phosphorylation and dynamin-endocytosis reduced v_{RMS} and ψ
206 to control levels (Figure 4D, Supplementary Movie 17). Additionally, RAB5A-cysts displayed
207 elevated phosphoERK1/2 (Supplementary Figure 7B) and straight and compact junctions
208 (Supplementary Figure 7C), indicating that, RAB5A impacts on similar biochemical and microscopic
209 determinants as in 2D monolayers[14].

We also noticed that inducing RAB5A expression in the initial phase of cystogenesis reduced the number of acini, but the ones remaining were significantly larger (Figure 4E-F), and did not undergo proliferation arrest, like control cysts do, as revealed by Ki67 staining or apoptosis (Supplementary Figure 7D). Importantly, proliferation was not a pre-requisite for motility, since treatment with Mitomycin C had no effects on rotations (Supplementary Movie 18). We investigated this phenotype further by inducing RAB5A expression at the end of morphogenesis, when fully-differentiated acini have ceased proliferation and motility[18]. RAB5A expression reawakened not only cell motility (Supplementary Movie 19) but also proliferation in an ERK1/2-dependent manner (Figure 4G-H).

The ERK1/2-dependent re-awakening of collective motion and proliferation of terminally-differentiated acini has been associated with the initiation of a more complex program of branched morphogenesis that begins with the formation of multicellular buds[40]. This process requires in addition to specific growth factors, also cell interaction with the microenvironment and ECM components[41, 42]. Collagen Type-I, for example, has been used to increase chemo-mechanical signalling and facilitate duct morphogenesis[43]. Henceforth, we grew MCF10A cells over mixed matrigel:collagen gels[42]. Under these conditions, RAB5A expression caused cysts to lose their spherical roundness, and promoted the formation of buds (Figure 4I-J).

Endocytic unjamming promotes carcinoma collective invasion

To determine whether RAB5A-unjamming can be exploited by breast cancer lines to enhance collective motility and invasiveness, we employed MCF10.DCIS.com cells, which are isogenic to MCF10A, express oncogenic T24-H-RAS and are used as models for the progression of DCIS to invasive carcinoma[44]. During the DCIS phase, cells grow under intra-ductal confinement where cell packing and density exert mechanical stress and supress tumour motility and progression. Consistently, MCF10.DCIS.com cells plated as confluent monolayers are kinetically-arrested. RAB5A expression promoted the reawakening of collective motion (Supplementary Figure 8A,

Supplementary Movie 20 and ref[14]), and accelerated wound closure of monolayers, which instead of arresting after the opposing fronts collided, kept on flowing, reminiscent of "a wound that never heals[45]" (Figure 5A-C, Supplementary Movie 21). Biochemically, RAB5A expression decreased total EGFR levels, but increased ERK1/2 without affecting AKT or p38 phosphorylation (Supplementary Figure 8B). Next, we monitored the kinematics of mCherry-H2B control and RAB5A-expressing MCF10.DCIS.com spheroids embedded into native collagen type-I by developing 3D Differential Variance Analysis (see Methods). Whereas control cells displayed a slow, uncorrelated, disordered motion (Figure 5D-E, Supplementary Figure 8C, Supplementary Movie 22), RAB5A-MCF10.DCIS.com cells acquired collective rotational motility, characterized by a large angular velocity Ω (of the order of ~12 rad/hr) and a strong orientational persistence of the instantaneous axis of rotation, captured by the decay time of the orientational correlation function (Figure 5E, Supplementary Figure 8C). We also observed a speed-up of the local cell rearrangement dynamics, estimated by calculating the overlap parameter $Q(\Delta t)$, which quantifies (see also Methods) the fraction of nuclei that have been displaced from their original position during a time interval of duration (Δt, when observed in a reference frame co-moving with the whole spheroid (Figure 5E, Supplementary Figure 8C). The decay of $Q(\Delta t)$ does not depend on the rigid motion of the spheroid as a whole, but captures, instead, the "fluid-like" relative motion of cells.

By repeating the same analysis in a space-resolved fashion (see Methods), we discovered that, for RAB5A-MCF10.DCIS.com spheroids, the decorrelation rate associated with the decay of the local overlap parameter displayed a systematic radial dependence, being much larger at the periphery of the spheroid (Figure 5F-G). The presence of a "melted" layer of cells on the surface of the rotating spheroid was confirmed by an optical-flow analysis (see Methods) of the velocity fluctuations (Supplementary Movie 23) that, after removal of the global rotation, exhibited a marked increase close to the boundaries (Figure 5F-G).

Endocytic-mediated liquid-like collective rotation in RAB5A-MCF10.DCIS.com spheroids was dependent on EGFR activity, ERK1/2 phosphorylation, Dynamin-2 and abrogated by inhibiting ARP2/3-mediated actin polymerization (Supplementary Figure 8C, Supplementary Movie 24). Furthermore, EM morphological analysis of monolayers, spheroids and orthotopically-injected tumours revealed that RAB5A expression induces junctional straightening and increases cell-cell contact areas (Figure 5H). Thus, similar cellular/biochemical processes driving 2D locomotion and acini morphogenesis control the dynamics of oncogenic epithelial ensembles.

Next, we explored the consequence of endocytic-mediated, unjamming by monitoring oncogenic spheroids co-expressing EGFP-LifeAct and mCherry-H2B over longer time scales. Invariably, RAB5A promoted collective angular motion and the formation of invasive, multicellular buds and strands, suggesting that unjamming and collective invasion might be temporally coordinated and possibly coupled (Figure 6A-B, Supplementary Movie 25).

Collective invasion into native collagen type-I, which, at the concentration used, form a dense fibrillar network (Supplementary Figure 8D), can only occur following its remodelling. To verify this, we exploited fluorescent functionalized-beads that bind to the collagen fibres, impeding relative motion between beads and the ECM used to embed the spheroids (Figure 6C, Supplementary Movie 26). We developed Stress Fluctuation Microscopy (see Methods) to infer, from the instantaneous velocity maps of the tracers (Supplementary Movie 27), an estimate of RMS values of the fluctuating strains induced by the cellular motion onto the ECM. Reconstructed normal RMS stresses are obtained (Figure 6D-E, Supplementary Movie 27) *via* the constitutive equations of the material, whose Young's modulus $E = 135 \pm 57\, Pa$ was measured using atomic-force microscopy (Supplementary Figure 8D). The RMS stresses imposed on the matrix by RAB5A-spheroids were about two times larger than controls (Figure 6E). The corresponding RMS normal strain at the boundary of RAB5A-expressing cells was of the order of about 10%, well above the critical value (strain ~ 5-6.5%) at which native collagen gels starts exhibiting a non-linear mechanical response and

284 strain-induced remodelling[46-48]. Consistently, RAB5A-expressing, rotating spheroids extensively
285 remodelled fibrillary collagen, detected by Second Harmonic Generation (SHG) signals of two-
286 photon illumination, generating gaps and channels (Supplementary Figure 8E). EGFR, ERK1/2,
287 Dynasore, and ARP2/3 inhibitor of collective angular motion prevented also collagen remodelling
288 and invasion (Figure 6F).

289 Next, we extended this finding using *ex vivo* organotypic tumour slices from m-Cherry-H2B and
290 EGFP-LifeAct-expressing DCIS orthotopically-injected into immunocompromised mice. Tumour
291 masses were mechanically excised and grown as organotypic tissue slices at the air-liquid interface
292 (see methods and ref.[49]). Whereas control tumours were immobile, jammed and compacted, RAB5A-
293 expressing malignant cells became highly motile and appeared to stream like a flowing liquid
294 (Supplementary Movie 28) also captured by PIV (Figure 6G-H, Supplementary Movie 29). Thus,
295 endocytic unjamming of kinetically-arrested DCIS tumours is sufficient to instigate motility and
296 promote collective invasion.

297 The pathophysiological relevance of our findings is underscored by the observations that RAB5A
298 is deregulated in breast cancer[13, 50], and specifically during the invasive progression of human ductal
299 breast carcinomas. Indeed, RAB5A expression was low in malignant cells of densely-packed and
300 jammed DCIS foci. The percentage of strongly expressing RAB5A cells increased at foci of DCIS
301 associated with invasive components or in overt infiltrating carcinomas (IDC) (Supplementary Figure
302 9A). Additionally, RAB5A increased expression was detected in aggressive breast cancer cell lines
303 (Supplementary Figure 9B), and correlated with worse relapse-free probability in various breast
304 cancer subtypes (Supplementary Figure 9C).

305

306 **Conclusions**

307 We identify a molecular route, which reinstates multicellular rearrangements in otherwise immobile
308 mature epithelia and densely-packed carcinoma. Biochemically, we showed that elevated RAB5A

309 enhances non-clathrin endocytosis of EGFR and promotes its accumulation into endosomal vesicles,
310 which become signalling platforms for the prolonged and elevated activation of ERK1/2. This, in
311 turn, is sufficient to promote the hyper-phosphorylation of WAVE2 that, by controlling actin
312 polymerization, contributes to the extension of oriented, cryptic lamellipodia[35]. Physically, the latter
313 protrusions exert increased traction forces[14, 51], and enhance cell orientation, promoting flocking in
314 epithelia monolayers and long-range coordinated rotation in 3D cysts and spheroids.

315 Remarkably, RAB5A-expressing spheroids display a radial gradient of fluidity whereby cells at
316 the periphery in contact with the ECM exhibit faster rearrangement dynamics and increased tissue
317 fluidization. These kinematic changes are linked to increased strains/stresses exerted on the
318 surrounding ECM beyond the threshold for remodelling fibrillar collagen[46], thereby facilitating to the
319 generation of tracks and channels into which fluidized cells advance collectively. These mechanical
320 changes are remarkably reminiscent to the graded unjamming (solid-to-fluid) transition observed
321 along the body axis of developing zebrafish embryo and shown to drive body axis elongation[52]. They
322 further point to the concept that spatio-temporal control of fluid-like and solid-like tissue states, and
323 graded fluidization specifically, might be a general physical mechanism of diverse multicellular
324 collectives. This mechanism might emerge as an adaptive "smart material" strategy of cell collectives
325 in responses to variation in the chemical/mechanical composition of the ECM and further impacts on
326 the structural composition of surrounding stroma. Within this context, the transition from DCIS,
327 which grow under intra-ductal confinement where extreme cell packing and density exert mechanical
328 stress and supress motility, to invasive carcinoma, which disperse locally also through collective
329 invasion[53], represents a case in point.

330 **Methods**

331 Methods and any associated accession codes and references are included after the references.

332

333 **Acknowledgments**

334 This work has been supported by: the Associazione Italiana per la Ricerca sul Cancro (AIRC) to GS
335 (IG#18621), PPDF (IG#18988 and MCO 10.000), and FG (MFAG#22083); the Italian Ministry of
336 University and Scientific Research (MIUR) to PPDF and GS (PRIN: PROGETTI DI RICERCA DI
337 RILEVANTE INTERESSE NAZIONALE – Bando 2017#2017HWTP2K); the Italian Ministry of
338 Health (RF-2013-02358446) to GS. Regione Lombardia and CARIPLO foundation (Project 2016-
339 0998) to RC; Worldwide Cancer Research (WCR#16-1245) to SS. CM and FG are partially supported
340 by fellowships from the University of Milan, EB from the FIRC-AIRC. We thank Joel Christian (Max
341 Planck Institute for Medical Research, Heidelberg, Germany) for help with fluorescent beads.

342

343

344 **Author contributions**

345 AP, CM, EF design and perform all the experiments and edited the manuscript, SC aid in generating
346 cell lines and in the analysis of IF and kinematic studies, EB, SS and PPFD conceived internalization
347 assays and interpreted trafficking results, GVB perform EM studies, EM, MG, and DP aided in all
348 the imaging acquisition, FRET and PIV analysis, CT aided in analysis of RAB5A expression in breast
349 cancer, QL and FA performed and analyzed AFM measurements, FG and RC analyzed all the
350 kinematic data, developed the tools for 3D motility and mechanical analysis, edited the manuscript
351 and conceived part of the study together with CM. EAC-A helped in setting the fluorescent beads
352 assay. GS conceived the whole study, wrote the manuscript and supervised the whole work.

353

354

355 **Competing financial interests**

356 The authors declare no competing financial interests.

357

358 **Data Availability Statement**

359 Codes used for the analysis are all indicated in the methods section. The authors declare that all data
360 supporting the findings of this study are available within the paper and its supplementary information
361 files and from the corresponding authors upon reasonable request.

Figure 1

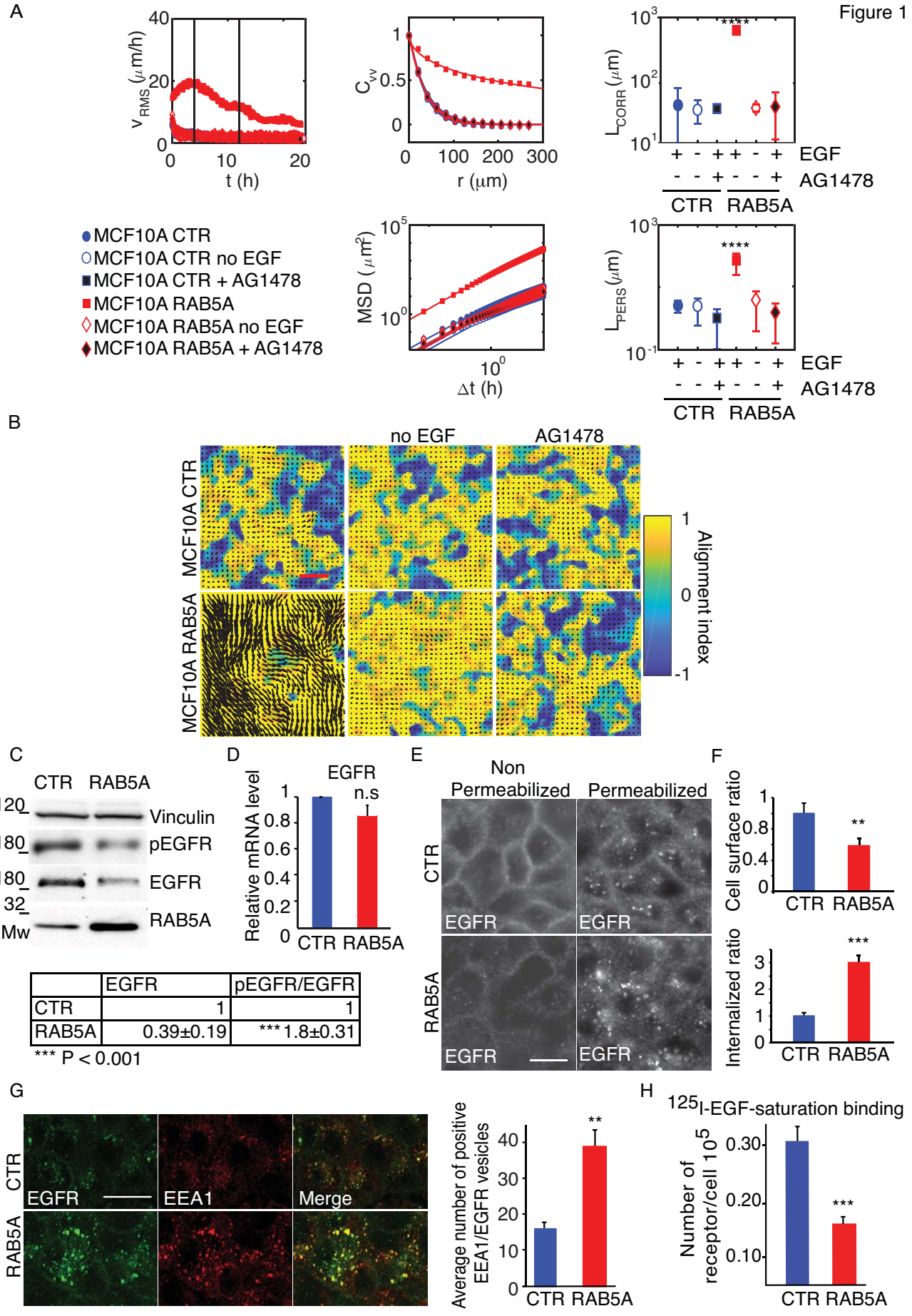

	EGFR	pEGFR/EGFR
CTR	1	1
RAB5A	0.39±0.19	*** 1.8±0.31

*** P < 0.001

Figure 1. Endocytic reawakening of motility is dependent on EGFR activation

A. PIV analysis of motion of control and RAB5A-expressing-MCF10A monolayers in the presence or the absence of EGF (Supplementary Movies 1 and 3) or the EGFR inhibitor AG1478 (Supplementary Movie 2). Vertical lines indicate the time interval used for the analysis of motility parameters: $v_{RMS} = \sqrt{\langle |\boldsymbol{v}|^2 \rangle}$: root mean square velocity; C_{VV}: velocity correlation functions as function of the distance r; L_{corr}: correlation lengths; MSD: mean square displacements obtained by numerical integration of the velocity maps over a given time interval, Δt.; $L_{pers,}$ persistence length. Data are from at least 5 movies/experimental conditions in 4 experiments.

B. Snapshots of the velocity field obtained from PIV analysis of motion of control (CTR) and RAB5A-MCF-10A monolayers treated as indicted (Supplementary Movie 4). The colour-map represents the alignment with respect to the mean instantaneous velocity, quantified by the parameter $a(x) = (\boldsymbol{v}(x) \cdot \boldsymbol{v}_0)/(|\boldsymbol{v}(x)||\boldsymbol{v}_0|)$. $a = 1(-1)$ when the local velocity is parallel (antiparallel) to the mean direction of migration. Bar, 100 μm.

C. Immunoblot of the indicated proteins and quantification of total EGFR and phosphorylated/total EGFR value. Data are expressed relative to control after normalizing to Vinculin (mean±SD, n=5 independent experiments)

D. Relative EGFR mRNA levels normalized to GAPDH (mean±SD, n=5 independent experiments).

E. Control and RAB5A-MCF10A were either permeabilized or non-permeabilized with 0.1% Triton X100 before staining.

F. Data are mean±SD of total cell surface or internalized EGFR relative to control normalized to cell number (n = 100 cells in 3 independent experiments). Bar, 20 μm.

G. Images of control and RAB5A-MCF10A monolayers stained with the indicated abs. Data are the mean±SD of EEA1 and EGFR-positive vesicles/cells (n>150 out of 3 independent experiments). Bar, 20 μm

387 **H**. Number of EGFR/cell measured by ^{125}I-EGF saturation binding after subtracting unspecific
388 background. Data are the mean±SD of triplicate measurements.
389 **p < 0.01, ***p < 0.001, each-pair Student's t-test.

Figure 2

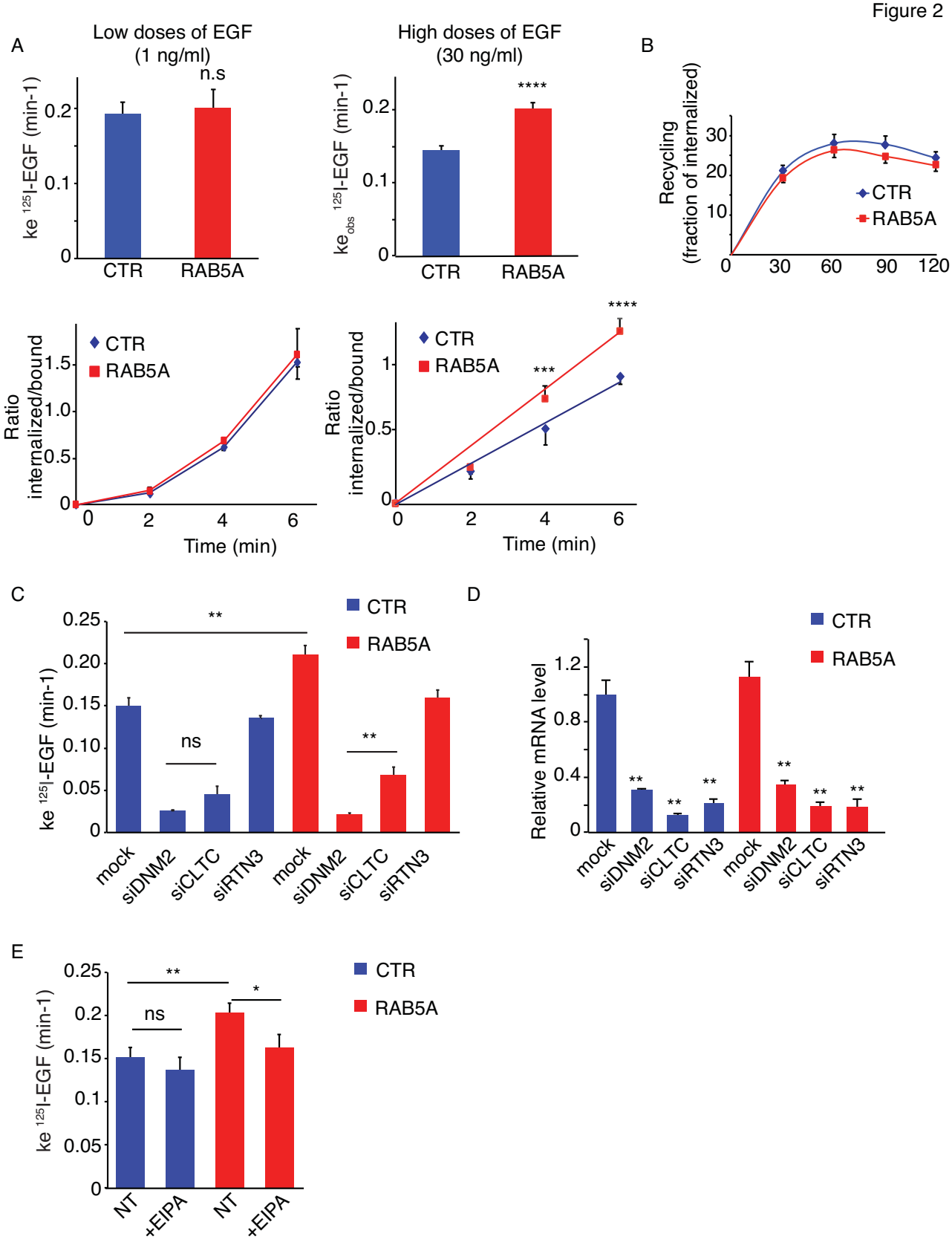

Figure 2. RAB5A increases non-Clathrin internalization of EGFR.

A. Effective or apparent internalization rate constants at low (1 ng/ml) or high (30 ng/ml) concentrations ^{125}I-EGF, respectively (Ke, upper panel) in control and RAB5A-expressing monolayers. A representative kinetic of the ratio of ^{125}I-EGF internalized/bound is shown and is expressed as the mean±SD (n=3 out of 12 independent experiments). ****p <0.0001. *P* values, each-pair Student's t-test.

B. Control or RAB5A-MCF10A cells monolayers were incubated with ^{125}I-EGF (30 ng/ml) for 15 min at 37 ˚C. Recycling of ^{125}I-EGF at the indicated time points was estimated as described in Methods. Data are the mean ± SD (n = 3 replicates in a representative experiment).

C. EGFR internalization kinetic in control and RAB5A-expressing monolayers silenced for Dynamin-2 (DNM2), Clathrin heavy chain (CLTC) or Reticulon 3 (RTN3) using ^{125}I-EGF at high (30 ng/ml) concentrations. Results are the mean±SD (n=3 independent experiments) of the apparent internalization rate constants, Ke. **p <0.01. *P* values, each-pair Student's t-test (the comparison between paired values is indicated). See Supplementary Table 2 for additional statistics.

D. The effectiveness of silencing was measured by QRT-PCR. Data are expressed relative to control after normalizing to GAPDH. The data are the relative level of gene expression compared to control expressed as mean ± SD (n=3 independent experiments). ** p < 0.01, *P* values, each-pair Student's t-test (siRNA vs control).

E. EGFR internalization kinetic in control and RAB5A-expressing cells monolayers treated with vehicle or 5-(N-ethyl-Nisopropyl) amiloride (EIPA) (75 μM) was measured using ^{125}I-EGF at high (30 ng/ml) concentrations. Results are mean±SD (n=3 independent experiments) of the apparent internalization rate constants, Ke. *p <0.05**, p <0.01. *P* values, each-pair Student's t-test (the comparison between each paired value is indicated).

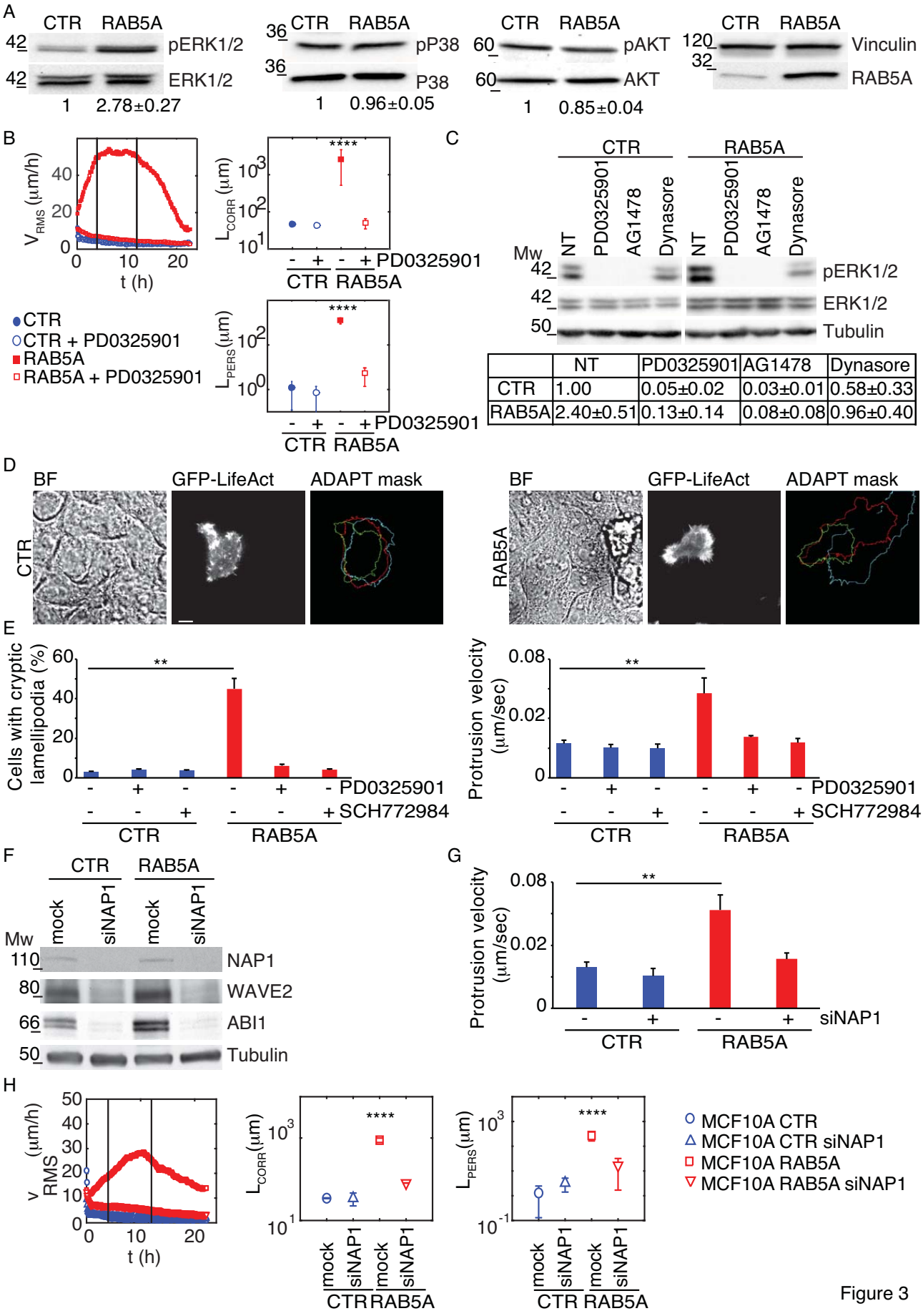
A
CTR RAB5A
42 pERK1/2
42 ERK1/2
1 2.78±0.27
36 pP38
36 P38
1 0.96±0.05
60 pAKT
60 AKT
1 0.85±0.04
120 Vinculin
32 RAB5A
B
V_{RMS} (µm/h)
t (h)
L_{CORR} (µm)
L_{PERS} (µm)
****
PD0325901
CTR RAB5A
CTR
CTR + PD0325901
RAB5A
RAB5A + PD0325901
C
CTR RAB5A
NT PD0325901 AG1478 Dynasore
Mw
42 pERK1/2
42 ERK1/2
50 Tubulin
NT PD0325901 AG1478 Dynasore
CTR 1.00 0.05±0.02 0.03±0.01 0.58±0.33
RAB5A 2.40±0.51 0.13±0.14 0.08±0.08 0.96±0.40
D
BF GFP-LifeAct ADAPT mask
CTR
RAB5A
E
Cells with cryptic lamellipodia (%)
Protrusion velocity (µm/sec)
**
PD0325901
SCH772984
CTR RAB5A
F
CTR RAB5A
mock siNAP1 mock siNAP1
Mw
110 NAP1
80 WAVE2
66 ABI1
50 Tubulin
G
Protrusion velocity (µm/sec)
**
siNAP1
CTR RAB5A
H
v_{RMS} (µm/h)
t (h)
L_{CORR} (µm)
L_{PERS} (µm)
****
mock siNAP1 mock siNAP1
CTR RAB5A
MCF10A CTR
MCF10A CTR siNAP1
MCF10A RAB5A
MCF10A RAB5A siNAP1

Figure 3

414

Figure 3. RAB5A endosomal ERK1/2 activity is required for flocking locomotion

A. Immunoblot of control and RAB5A-MCF10A monolayers with the indicated abs. The ratio of phosphorylated/total levels of the indicated proteins is expressed mean±SD (n=5 independent experiments).

B. PIV analysis of motion (Supplementary Movie 8) of control and RAB5A-MCF10A monolayers treated with vehicle or PD0325901 (1 μM), a MEK inhibitor to extract: root mean square velocity $V_{RMS} = \sqrt{\langle |\boldsymbol{v}|^2 \rangle}$, correlation length L_{corr} and persistence length L_{pers}. Data are the mean±SD (n=5 movies/ conditions out of 3 independent experiments).

C. Immunoblot of control and RAB5A-MCF10A monolayers treated with PD0325901, or AG1478, or Dynasore (80 μM) or vehicle as control with the indicated abs. The ratio of phosphoERK1/2/totalERK1/2 is expressed as mean±SD (n=4 independent experiments).

D-E. Still phase-contrast and fluorescent images of cryptic lamellipodia in control and RAB5A-MCF-10A monolayers composed of mosaically GFP-LifeAct-expressing (green):non-expressing cells (1:10 ratio) from Supplementary Movie 11. Examples of the fluctuation of cell contours at 0'-green, 45'-red, 90'-indaco (ADAPT Mask). Bars, 20 μm. In **E**, Number of cells with lamellipodium and velocity of protrusion fluctuation are expressed as mean±SD. (n=65 cells/conditions from 4 independent experiments).

F. Immunoblotting of control and RAB5A-MCF10A cells monolayers silenced for the critical WAVE complex component, NAP1.

G. Analysis of the dynamics of cell protrusions of mosaically-expressing GFP-lifeAct, control and RAB5A-MCF10A monolayers silenced for the critical WAVE complex component, NAP1, Supplementary Movie 12. The velocity of protrusion fluctuation is the mean±SD (n=96 cells/conditions from 3 independent experiments).

H. PIV analysis of motion (Supplementary Movie 13) of control and RAB5A-MCF10A monolayers silenced for the critical WAVE complex component, NAP1, to extract: root mean square velocity

440 $V_{RMS} = \sqrt{\langle |\boldsymbol{v}|^2 \rangle}$, correlation length L_{corr} and persistence length L_{pers}. Data are the mean±SD (n=5

441 movies/ conditions out of 3 independent experiments).

442 *p < 0.01, ****p < 0.0001, *P* values, each-pair Student's t-test.

443

444

445

Figure 4

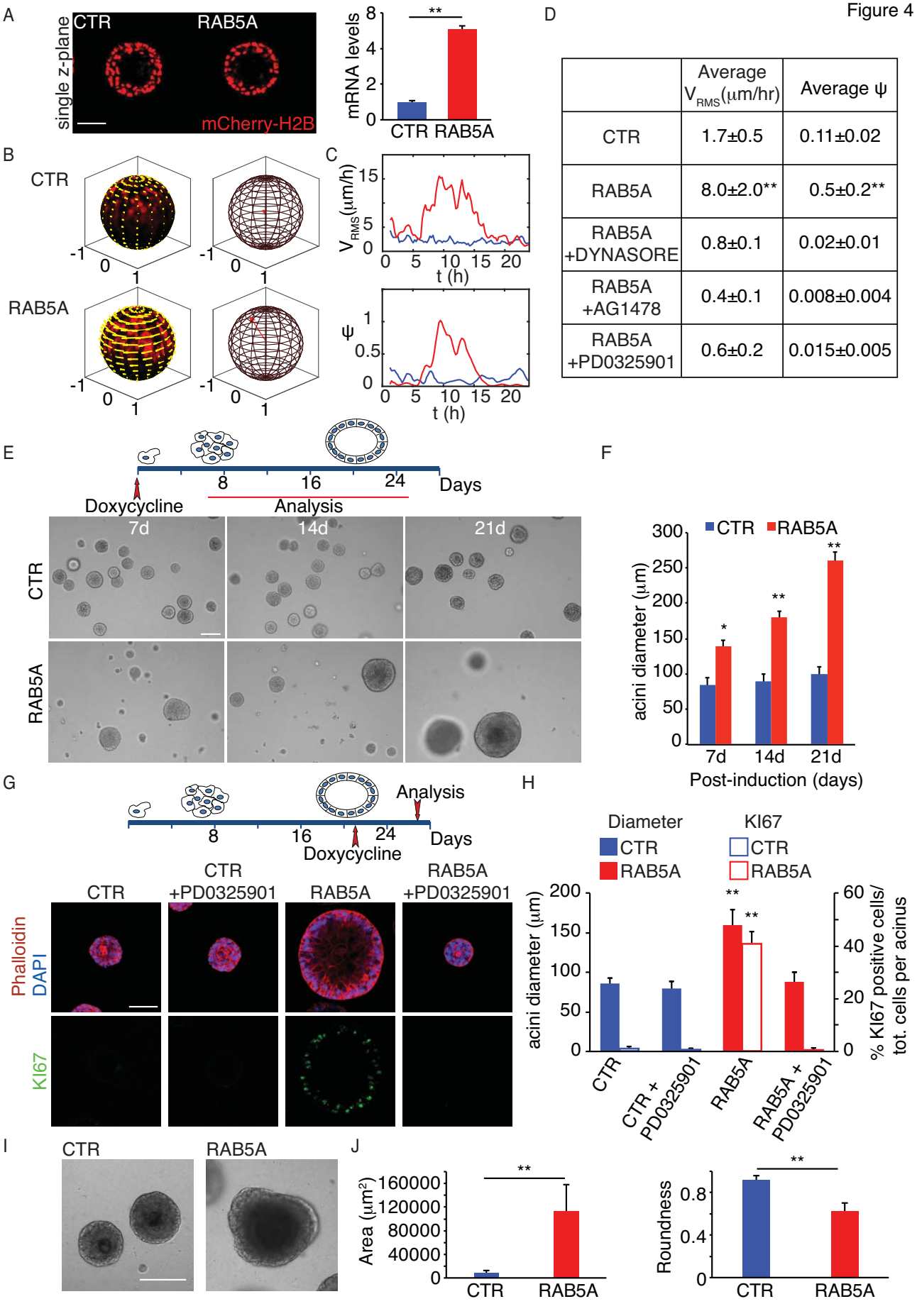

D

	Average V_{RMS}(μm/hr)	Average ψ
CTR	1.7±0.5	0.11±0.02
RAB5A	8.0±2.0**	0.5±0.2**
RAB5A +DYNASORE	0.8±0.1	0.02±0.01
RAB5A +AG1478	0.4±0.1	0.008±0.004
RAB5A +PD0325901	0.6±0.2	0.015±0.005

Figure 4. RAB5A overcomes kinetic and proliferation arrest in terminally-differentiated acini.

A-C. Single Z planes from Supplementary Movie 15 of control and RAB5A-MCF10A-expressing mCherry-H2B acini. RAB5A mRNA levels relative to control after normalizing to GAPDH are shown as mean±SD (n=3 independent experiments). Bar, 50 μm. In **B**, Tangential velocity fields at t = 10 h (yellow arrows) from PIV analysis, overlaid on radial projection of acini onto a unit spherical surface (Supplementary Movie 16). The red arrow is parallel to the instantaneous total angular momentum $\boldsymbol{l}$ and provides the orientation of the instantaneous axis of rotation. Its length is equal to the instantaneous order parameter ψ. In **C**, Time evolution of root mean square velocity v_{RMS} and rotational order parameter ψ (see text and Methods) representative of 4 movies in 3 experiments.

D. $V_{RMS} = \sqrt{\langle |\boldsymbol{v}|^2 \rangle}$ and of ψ, calculated over the 4-to-12 h (Supplementary Movie 17) time window for control and RAB5A-MCF-10A mcherry-H2B- expressing MCF10A acini treated as indicated. Average values are from 5 movies in 3 independent experiments.

E. Control and RAB5A-MCF10A acini treated as indicated above were processed for phase contrast imaging to monitor acini shape and size (left images). Bar, 100 μm.

F. Acini size expressed as the mean±SD (n=100 acini/conditions in 5 independent experiments).

G. IF images of control and RAB5A-MCF10A acini treated with doxycycline as indicated in the presence or absence of PD0325901. Bar, 80 μm.

H. Acini diameter and the number of KI67+ cells/ total number of cells/ acini is reported as means±SD (n=25 acini/conditions in 3 independent experiments).

I. Control and RAB5A-MCF10A acini grown on mixed 1:1=Matrigel:Collagen Type-I plugs for 21 days were processed for phase contrast imaging. Bar, 100 μm.

J. Acini area and roundness is expressed as mean±SD (n=40 acini/conditions in 5 experiments).

*p<0.05, ** p < 0.01. P values, each-pair Student's t-test.

Figure 5

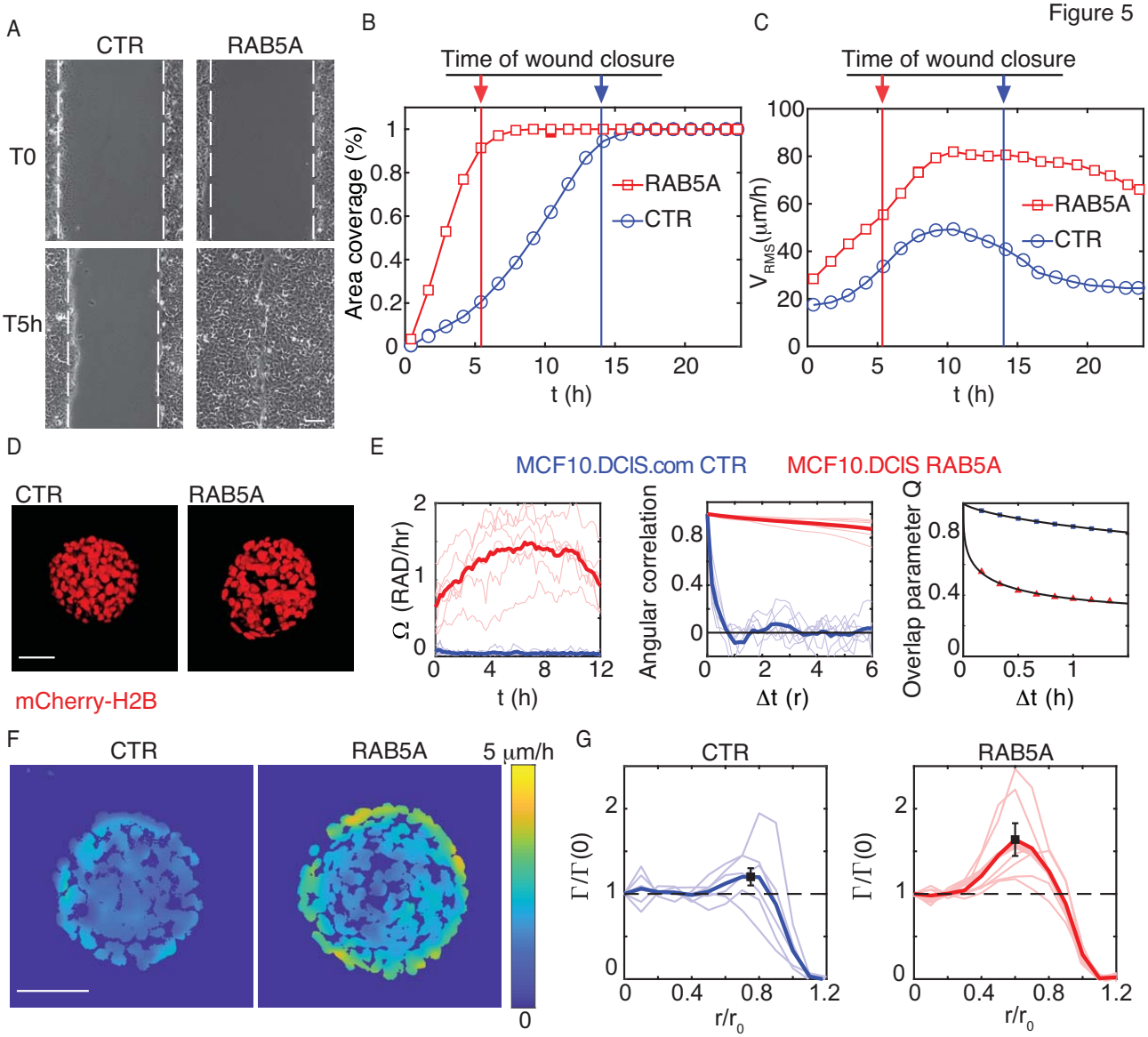

0.45±0.14	0.79±0.23	0.83±0.21		0.13±0.05****	0.09±0.03****	0.08±0.02****
Average cell-cell membrane distance (μm)						

471

Figure 5. RAB5A promotes the emergence of coordinated angular rotation in cancer spheroids

A-C. Stills of scratched wound migration in control and RAB5A-MCF10.DCIS.com monolayers. Dashed lines mark the wound edges. Bar, 100 μm. Motility (Supplementary Movie 21) was quantified as (**B**) the percentage of area covered or (**C**) $V_{RMS} = \sqrt{\langle |\boldsymbol{v}|^2 \rangle}$. Vertical bars indicate the time at which wounds closed. Data are representative of 1 experiment out of >10.

D-E. Snapshots of mCherry-H2B-expressing, control and RAB5A-MCF10.DCIS.com spheroids embedded in Collagen Type-I (6.0 mg/ml). Bar, 100 μm. **E**. Image Differential Variance-based Analysis (3D DVA) of 5-8 spheroid/conditions in 3 independent experiments (Methods and Supplementary Movie 22) was performed to extract: the angular velocity Ω (rad/hr); the angular correlation of motion quantified by considering the decay of the orientational correlation function; the overlap parameter Q captured from the non-rigid part of motion, involving mutual cell rearrangement and fluid-like dynamics.

F-G. Maps of the RMS velocity fluctuations on the equatorial plane of a CTR and RAB5A-expressing spheroid. Bar, 100 μm. In **G**, azimuthally averaged radial profiles of the relaxation rate Γ, for CTR and RAB5A spheroids, obtained with 3D DVA analysis (Supplementary Movie 23). Curves are scaled along the x axis with the radius r_0 of each spheroid and along the y axis with the value of the relaxation rate $\Gamma(0)$ at the center of spheroid. Thick curves represent the average value with peacks at 1.2±01 and 1.6±0.2. (n=7 for each condition). $p<0.05$, each-paired Student's *t*-test.

H. Electron microscopy of control and RAB5A-MCF10.DCIS.com monolayers, or 3D spheroids, or tumor orthotopically injected into immune-compromised mice. Blue arrows point to cell–cell contact spaces, red arrows to tight cell–cell contacts. Bar, 2 μm. The average distance between adjacent cells is reported below as mean±SD (n=35 cell-cell junction in random fields in 3 experiments). **** $p < 0.001$. P values, each-pair Student's t-test.

Figure 6

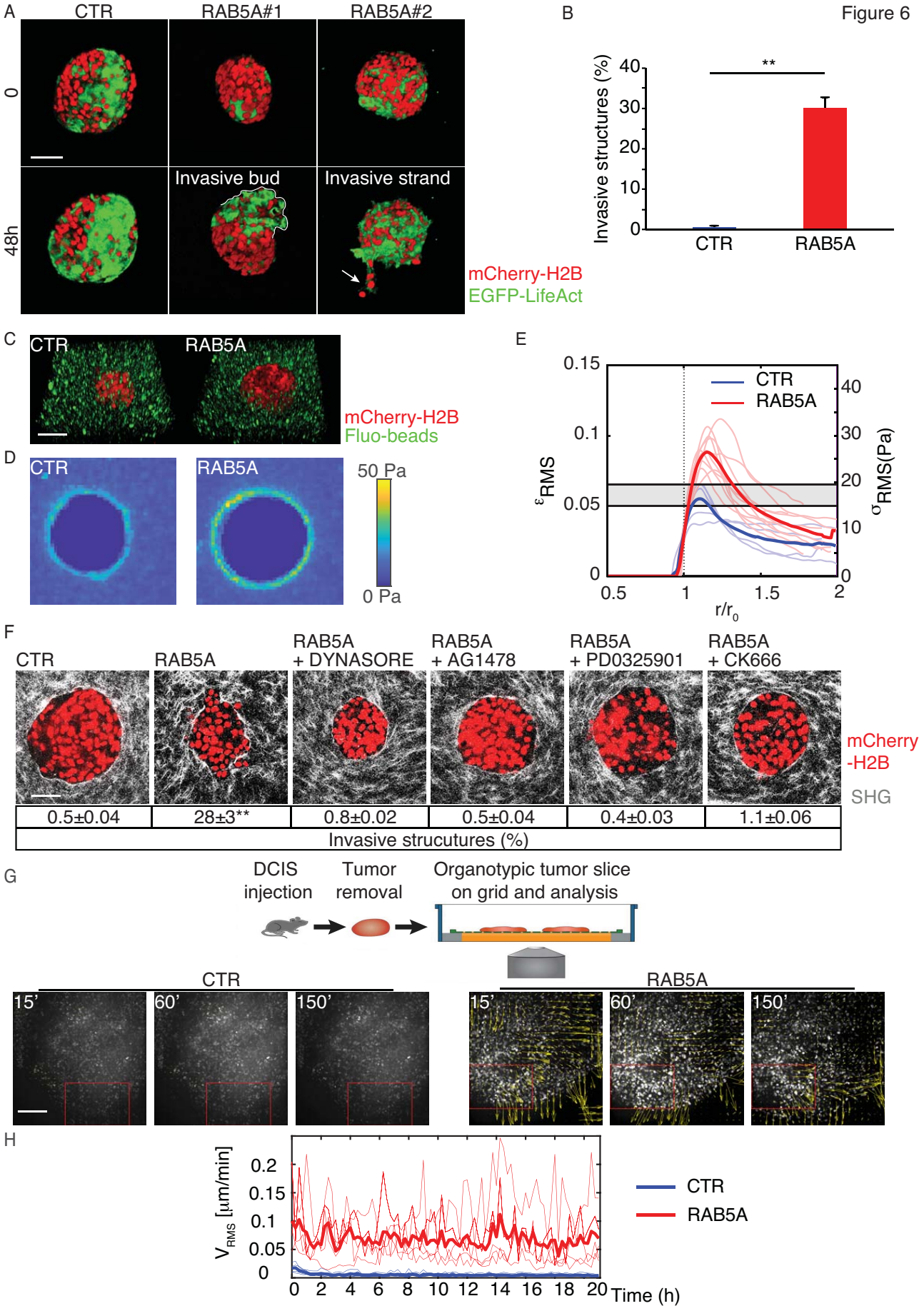
A
CTR
RAB5A#1
RAB5A#2
0
48h
Invasive bud
Invasive strand
mCherry-H2B
EGFP-LifeAct
B
Invasive structures (%)
40
30
20
10
0
**
CTR
RAB5A
C
CTR
RAB5A
mCherry-H2B
Fluo-beads
D
CTR
RAB5A
50 Pa
0 Pa
E
0.15
0.1
0.05
0
εRMS
CTR
RAB5A
40
30
20
10
0
σRMS(Pa)
0.5
1
1.5
2
r/r0
F
CTR
RAB5A
RAB5A + DYNASORE
RAB5A + AG1478
RAB5A + PD0325901
RAB5A + CK666
mCherry -H2B
SHG
0.5±0.04
28±3**
0.8±0.02
0.5±0.04
0.4±0.03
1.1±0.06
Invasive strucutures (%)
G
DCIS injection
Tumor removal
Organotypic tumor slice on grid and analysis
CTR
RAB5A
15’
60’
150’
H
VRMS [μm/min]
0.2
0.15
0.1
0.05
0
0 2 4 6 8 10 12 14 16 18 20
Time (h)
CTR
RAB5A

Figure 6. RAB5A promotes collective invasion in tumour spheroids and tumours slices

A-B. Invasive structures in EGFP-LifeAct and mCherry-H2B-co-expressing control and RAB5A-MCF10.DCIS.com spheroids embedded in Collagen Type-I (Supplementary Movie 25). The line delineates an invasive multicellular bud; the arrow points to an invasive strand. The percentage of spheroids with invasive structures is expressed as mean±SD (n=15/experimental conditions in 5 independent experiments). ** p<0.01, each-paired Student's t-test Bar, 150 μm.

C. Snapshots (Supplementary Movie 26) of mCherry-H2B-expressing control and RAB5A-MCF10.DCIS.com spheroids embedded in Collagen Type-I interspersed with functionalized fluorescent-beads (Fluo-beads). Bar, 200 μm.

D. Maps of RMS normal stresses on ECM in the equatorial plane of CTR and RAB5A-expressing spheroids, respectively (Supplementary Movie 27).

E. Azimuthally averaged radial profiles of the RMS normal stress/strain for CTR and RAB5A-spheroids. Curves are scaled along the x axis with the radius r_0 of each spheroid. Thick curves are the average of analyzed spheroids. The shaded region corresponds to the critical strain above which Collagen undergoes strain-induced structural remodelling and non-linear mechanical response[46]. p < 0.01, pair Student's *t*-test.

F. SHG analysis of Collagen type-I fibres used to embed mCherry-H2B-expressing control and RAB5A-MCF10.DCIS.com spheroids in the presence of vehicle or the indicated inhibitors. The % of spheroids with invasive structures is expressed as mean±SD (n=15/experimental conditions in 5 independent experiments). ** p<0.01, each-pair Student's t-test. Bar, 70 μm.

G-H. Experimental scheme: EGFP-LifeAct and mCherry-H2B-expressing control and RAB5A-MCF10.DCIS.com DCIS orthotopically-injected into immunocompromised mice were mechanically excised and placed at the air-liquid interface, and monitored by time-lapse (Supplementary Movie 28). PIV analysis to extract the cellular root mean square velocity, $V_{RMS} = \sqrt{\langle |\boldsymbol{v}|^2 \rangle}$ (Supplementary Movie 29). Boxed areas indicate fields of view for the analysis (At least 5

field of view/movie for 3 independent experiments). Bar, 150 μm. In **H**, thick lines are averages of the time-dependent V_{RMS} for each field of view (thin lines) in CTR and RAB5A, respectively.

References

1. Hakim, V. & Silberzan, P. Collective cell migration: a physics perspective. *Rep Prog Phys* **80**, 076601 (2017).
2. Haeger, A., Wolf, K., Zegers, M.M. & Friedl, P. Collective cell migration: guidance principles and hierarchies. *Trends Cell Biol* **25**, 556-566 (2015).
3. Park, J.A., Atia, L., Mitchel, J.A., Fredberg, J.J. & Butler, J.P. Collective migration and cell jamming in asthma, cancer and development. *J Cell Sci* **129**, 3375-3383 (2016).
4. Bi, D., Yang, X., Marchetti, M.C. & Manning, M.L. Motility-Driven Glass and Jamming Transitions in Biological Tissues. *Physical Review X* **6**, 021011 (2016).
5. Sadati, M., Taheri Qazvini, N., Krishnan, R., Park, C.Y. & Fredberg, J.J. Collective migration and cell jamming. *Differentiation; research in biological diversity* **86**, 121-125 (2013).
6. Atia, L. *et al.* Geometric constraints during epithelial jamming. *Nat Phys* **14**, 613-620 (2018).
7. Garcia, S. *et al.* Physics of active jamming during collective cellular motion in a monolayer. *Proc Natl Acad Sci U S A* **112**, 15314-15319 (2015).
8. Oswald, L., Grosser, S., Smith, D.M. & Kas, J.A. Jamming transitions in cancer. *J Phys D Appl Phys* **50**, 483001 (2017).
9. Haeger, A., Krause, M., Wolf, K. & Friedl, P. Cell jamming: collective invasion of mesenchymal tumor cells imposed by tissue confinement. *Biochim Biophys Acta* **1840**, 2386-2395 (2014).
10. Sigismund, S. & Scita, G. The 'endocytic matrix reloaded' and its impact on the plasticity of migratory strategies. *Curr Opin Cell Biol* **54**, 9-17 (2018).
11. Corallino, S., Malabarba, M.G., Zobel, M., Di Fiore, P.P. & Scita, G. Epithelial-to-Mesenchymal Plasticity Harnesses Endocytic Circuitries. *Frontiers in oncology* **5**, 45 (2015).
12. Palamidessi, A. *et al.* Endocytic trafficking of Rac is required for the spatial restriction of signaling in cell migration. *Cell* **134**, 135-147 (2008).
13. Frittoli, E. *et al.* A RAB5/RAB4 recycling circuitry induces a proteolytic invasive program and promotes tumor dissemination. *J Cell Biol* **206**, 307-328 (2014).
14. Malinverno, C. *et al.* Endocytic reawakening of motility in jammed epithelia. *Nature materials* **16**, 587-596 (2017).
15. Giavazzi, F. *et al.* Giant fluctuations and structural effects in a flocking epithelium. *Journal of Physics D: Applied Physics* **50**, 384003 (2017).
16. Giavazzi, F. *et al.* Flocking transitions in confluent tissues. *Soft matter* **14**, 3471-3477 (2018).
17. Mendoza, M.C. Phosphoregulation of the WAVE regulatory complex and signal integration. *Semin Cell Dev Biol* **24**, 272-279 (2013).
18. Debnath, J., Muthuswamy, S.K. & Brugge, J.S. Morphogenesis and oncogenesis of MCF-10A mammary epithelial acini grown in three-dimensional basement membrane cultures. *Methods* **30**, 256-268 (2003).
19. Levitzki, A. & Gazit, A. Tyrosine kinase inhibition: an approach to drug development. *Science* **267**, 1782-1788 (1995).

20. Lang, E. *et al.* Coordinated collective migration and asymmetric cell division in confluent human keratinocytes without wounding. *Nature communications* **9**, 3665 (2018).
21. Zeigerer, A. *et al.* Rab5 is necessary for the biogenesis of the endolysosomal system in vivo. *Nature* **485**, 465-470 (2012).
22. Kirchhausen, T., Owen, D. & Harrison, S.C. Molecular structure, function, and dynamics of clathrin-mediated membrane traffic. *Cold Spring Harbor perspectives in biology* **6**, a016725 (2014).
23. Sigismund, S. *et al.* Clathrin-mediated internalization is essential for sustained EGFR signaling but dispensable for degradation. *Dev Cell* **15**, 209-219 (2008).
24. Johannes, L., Parton, R.G., Bassereau, P. & Mayor, S. Building endocytic pits without clathrin. *Nat Rev Mol Cell Biol* **16**, 311-321 (2015).
25. Caldieri, G. *et al.* Reticulon 3-dependent ER-PM contact sites control EGFR nonclathrin endocytosis. *Science* **356**, 617-624 (2017).
26. Koivusalo, M. *et al.* Amiloride inhibits macropinocytosis by lowering submembranous pH and preventing Rac1 and Cdc42 signaling. *J Cell Biol* **188**, 547-563 (2010).
27. Di Guglielmo, G.M., Baass, P.C., Ou, W.J., Posner, B.I. & Bergeron, J.J. Compartmentalization of SHC, GRB2 and mSOS, and hyperphosphorylation of Raf-1 by EGF but not insulin in liver parenchyma. *EMBO J* **13**, 4269-4277 (1994).
28. Vieira, A.V., Lamaze, C. & Schmid, S.L. Control of EGF receptor signaling by clathrin-mediated endocytosis. *Science* **274**, 2086-2089 (1996).
29. McDonald, P.H. *et al.* Beta-arrestin 2: a receptor-regulated MAPK scaffold for the activation of JNK3. *Science* **290**, 1574-1577 (2000).
30. Villasenor, R., Nonaka, H., Del Conte-Zerial, P., Kalaidzidis, Y. & Zerial, M. Regulation of EGFR signal transduction by analogue-to-digital conversion in endosomes. *eLife* **4** (2015).
31. Barrett, S.D. *et al.* The discovery of the benzhydroxamate MEK inhibitors CI-1040 and PD 0325901. *Bioorg Med Chem Lett* **18**, 6501-6504 (2008).
32. Kirchhausen, T., Macia, E. & Pelish, H.E. Use of dynasore, the small molecule inhibitor of dynamin, in the regulation of endocytosis. *Methods Enzymol* **438**, 77-93 (2008).
33. Komatsu, N. *et al.* Development of an optimized backbone of FRET biosensors for kinases and GTPases. *Mol Biol Cell* **22**, 4647-4656 (2011).
34. Itoh, F. *et al.* The FYVE domain in Smad anchor for receptor activation (SARA) is sufficient for localization of SARA in early endosomes and regulates TGF-beta/Smad signalling. *Genes to cells : devoted to molecular & cellular mechanisms* **7**, 321-331 (2002).
35. Farooqui, R. & Fenteany, G. Multiple rows of cells behind an epithelial wound edge extend cryptic lamellipodia to collectively drive cell-sheet movement. *J Cell Sci* **118**, 51-63 (2005).
36. Alekhina, O., Burstein, E. & Billadeau, D.D. Cellular functions of WASP family proteins at a glance. *J Cell Sci* **130**, 2235-2241 (2017).
37. Mendoza, M.C. *et al.* ERK-MAPK drives lamellipodia protrusion by activating the WAVE2 regulatory complex. *Mol Cell* **41**, 661-671 (2011).
38. Innocenti, M. *et al.* Abi1 is essential for the formation and activation of a WAVE2 signalling complex. *Nat Cell Biol* **6**, 319-327 (2004).
39. Steffen, A. *et al.* Sra-1 and Nap1 link Rac to actin assembly driving lamellipodia formation. *Embo J* **23**, 749-759 (2004).
40. Ewald, A.J., Brenot, A., Duong, M., Chan, B.S. & Werb, Z. Collective epithelial migration and cell rearrangements drive mammary branching morphogenesis. *Dev Cell* **14**, 570-581 (2008).
41. Kim, H.Y. & Nelson, C.M. Extracellular matrix and cytoskeletal dynamics during branching morphogenesis. *Organogenesis* **8**, 56-64 (2012).
42. Carey, S.P., Martin, K.E. & Reinhart-King, C.A. Three-dimensional collagen matrix induces a mechanosensitive invasive epithelial phenotype. *Scientific reports* **7**, 42088 (2017).

43. Nguyen-Ngoc, K.V. *et al.* ECM microenvironment regulates collective migration and local dissemination in normal and malignant mammary epithelium. *Proc Natl Acad Sci U S A* **109**, E2595-2604 (2012).
44. Miller, F.R., Santner, S.J., Tait, L. & Dawson, P.J. MCF10DCIS.com xenograft model of human comedo ductal carcinoma in situ. *Journal of the National Cancer Institute* **92**, 1185-1186 (2000).
45. Dvorak, H.F. Tumors: wounds that do not heal. Similarities between tumor stroma generation and wound healing. *N Engl J Med* **315**, 1650-1659 (1986).
46. Vader, D., Kabla, A., Weitz, D. & Mahadevan, L. Strain-induced alignment in collagen gels. *PLoS One* **4**, e5902 (2009).
47. Storm, C., Pastore, J.J., MacKintosh, F.C., Lubensky, T.C. & Janmey, P.A. Nonlinear elasticity in biological gels. *Nature* **435**, 191-194 (2005).
48. Munster, S. *et al.* Strain history dependence of the nonlinear stress response of fibrin and collagen networks. *Proc Natl Acad Sci U S A* **110**, 12197-12202 (2013).
49. Staneva, R., Barbazan, J., Simon, A., Vignjevic, D.M. & Krndija, D. Cell Migration in Tissues: Explant Culture and Live Imaging. *Methods Mol Biol* **1749**, 163-173 (2018).
50. Yang, P.S. *et al.* Rab5A is associated with axillary lymph node metastasis in breast cancer patients. *Cancer Sci* **102**, 2172-2178 (2011).
51. Das, T. *et al.* A molecular mechanotransduction pathway regulates collective migration of epithelial cells. *Nat Cell Biol* **17**, 276-287 (2015).
52. Mongera, A. *et al.* A fluid-to-solid jamming transition underlies vertebrate body axis elongation. *Nature* **561**, 401-405 (2018).
53. Dang, T.T., Esparza, M.A., Maine, E.A., Westcott, J.M. & Pearson, G.W. DeltaNp63alpha Promotes Breast Cancer Cell Motility through the Selective Activation of Components of the Epithelial-to-Mesenchymal Transition Program. *Cancer Res* **75**, 3925-3935 (2015).

METHODS

Plasmids, antibodies and reagents.

Doxycycline-inducible lentiviral vectors pSLIK-neomycin (neo) carrying RAB5A or RAB5C sequences and pSLIK-hygromycin (hygro) carrying RAB5B sequence were obtained by Gataway Technology (Invitrogen), following the manufacturer's protocol. The plasmids pBABE-puromycin (puro)-mCHERRY-H2B and pBABE- puro-EGFP-H2B were provided by IFOM-Imaging Facility. The lentiviral expression construct pRRL-Lifeact-EGFP-puromicin (puro) was a gift of Olivier Pertz (University of Basel, Basel, Switzerland). pBabe-Puro-MEK-S218D/S222D (MEK-DD) vector was purchased from Addgene.

FRET EKAREV-ERK1/2 sensor[53] was generated by cloning synthetized FYVE domain of SARA into the BamHI/EcoRI cleaved EKAREV-FRET vector to generate pPBbsr2-3560NES-EKAREV-FRET vector.

Mouse monoclonal antibodies raised against α−tubulin (#T5168) or vinculin (#V9131) were from Sigma-Aldrich (dilution 1:400). Rabbit polyclonal anti-RAB5A (S-19, #sc-309) and goat polyclonal anti-EEA-1 (N-19, #sc-6415) antibodies from Santa Cruz Biotechnology (Dilution 1:400). Monoclonal rabbit anti-human RAB5A - ab109534, dilution 1:100, (Abcam[EPR5438]) was used of IHC;Rabbit polyclonal anti-Giantin (#PRB-114C) antibody was from Covance. Mouse monoclonal anti-human Ki-67 Antigen (MIB-1, #M7240) antibody was from Dako (1:1000). Mouse monoclonal anti-AP50 (AP2mu) (31/AP50, #611350) was from BD Bioscience. Mouse monoclonal anti-E-cadherin (#610181) antibody was from Transduction Lab (Dilution 1:1000). Rabbit polyclonal anti-phospho-EGFR (Tyr1086, #2220), rabbit monoclonal anti-phospho-p44/42 MAPK (ERK1/2) (Thr202/Tyr204, #4370), rabbit polyclonal anti-p44/42 MAPK (ERK1/2) (#9102), rabbit monoclonal anti-phospho-p38 MAPK (Thr180/Tyr182, 3D7, #9215), mouse monoclonal anti-p38 MAPK (L53F8, #9228), rabbit monoclonal anti-phospho-AKT (Ser473, 193H12, #4058), rabbit polyclonal anti-AKT (#9272), rabbit polyclonal anti-MEK1/2 (#9122) and rabbit polyclonal anti-cleaved

Caspase-3 (Asp175, #9661) antibodies were from Cell Signalling Technology (Dilution 1:1000). Rabbit polyclonal anti-phospho-WAVE2 (Ser343, #07-1512), rabbit polyclonal anti-phospho-WAVE2 (Ser351, #07-1514) and mouse monoclonal anti-Laminin-V (P3H9-2, #MAB1947) antibodies were from Merck/Millipore (Dilution 1:500). Mouse monoclonal anti-WAVE2 and mouse monoclonal anti-ABI1 antibodies were homemade[54] (Dilution 1:100). Rabbit polyclonal anti-NAP1 antibody was a gift of Theresia Stradal (Helmholtz Centre for Infection Research, Braunschweig, Germany)[55]. Rabbit polyclonal anti EGFR (806), directed against aa 1172-1186 of human EGFR (ImmunoBlot) and mouse monoclonal anti-EGFR (m108 hybridoma) directed against the extracellular domain of human EGFR (IF) were a gift from P.P. Di Fiore (Dilution 1:1000). Secondary antibodies conjugated to horseradish peroxidase were all used at dilution 1:2000 and were from: Bio-Rad (#7074, #7076); Cy3-secondary antibodies from Jackson ImmunoResearch (#711-165-152, #715-165-150); DAPI (#D-1306) and AlexaFluor 488 (A-11055, A-21202) were from Thermo Fisher Scientific. TRITC- (#P1951) and FITC-(#P5282) conjugated phalloidin were from Sigma Aldrich.

Doxycycline Hyclate (DOX, #D9891), Dynasore Hydrate (#D7693), AG1478 (#T4182), 5-(N-Ethyl-N-isopropyl)amiloride (#1154-25-2) and CK666 (#SML0006) were from Sigma Aldrich. PD0325901 (#444966) was from Merck/Millipore. SCH772984 (#942183-80-4) was from Selleckchem. FluoSpheres™ Sulfate Microspheres, 0.2 µm yellow-green fluorescent (505/515), 2% solids (#F8848) were from ThermoFisher. Mitomycin C (#M0503) from Sigma Aldrich.

Cell cultures and transfection.

MCF10A cells were a kind gift of J. S. Brugge (Department of Cell Biology, Harvard Medical School, Boston, USA) and were maintained in Dulbecco's Modified Eagle Medium: Nutrient Mixture F-12 (DMEM/F12) medium (Biowest) supplemented with 5% horse serum, 1% L-Glutamine (EuroClone), 0.5 mg ml^{-1}hydrocortisone (Sigma-Aldrich), 100 ng ml^{-1} cholera toxin (Sigma-Aldrich),

10 μg ml^{-1} insulin (Sigma-Aldrich) and 20 ng ml^{-1} EGF (Vinci Biochem). MCF10.DCIS.com cells were kindly provided by J. F. Marshall (Barts Cancer Institute, Queen Mary University of London, UK) and maintained in Dulbecco's Modified Eagle Medium: Nutrient Mixture F-12 (DMEM/F12) medium supplemented with 5% horse serum, 1% L-Glutamine, 0.5 mg ml^{-1}hydrocortisone, 10 μg ml^{-1} insulin and 20 ng ml^{-1} EGF. All cell lines have been authenticated by cell fingerprinting and tested for mycoplasma contamination. Cells were grown at 37 °C in humidified atmosphere with 5% CO_2. Phoenix-AMPHO (ATCC® CRL-3213™) were used as packaging cell line for the generation of retroviral particles and cultured as recommended by the supplier. HEK293T were obtained from BBCF-Biological Bank and Cell factory, INT, Milan grown in DMEM, 10% foetal bovine serum, 2mM L-Glutamine and used as packaging line for lentiviral vectors. MCF10A cells were infected with pSLIK-neo-EV (empty vector-CTR), pSLIK-neo-RAB5A, pSLIK-hygro-RAB5B or pSLIK-neo-RAB5C lentiviruses and selected with the appropriate antibiotic to obtain stable inducible cell lines. MCF10.DCIS.com were infected with pSLIK-neo-EV (empty vector-CTR) or pSLIK-neo-RAB5A lentiviruses and selected with the appropriate antibiotic to obtain stable inducible cell lines. Constitutive expression of EGFP-LifeAct- or mCHERRY- or EGFP-H2B was achieved by lentiviral and retroviral infection of MCF10A and MCF10DCIS.com cells with EGFP-LifeAct-puro or pBABE- puro-mCHERRY-H2B/ pBABE- puro-EGFP-H2B vectors, respectively.

Transfections were performed using either calcium phosphate or FUGENE HD Transfection reagent (#E2311, PROMEGA) reagents, according to manufacturer's instructions. FUGENE HD reagent was used for FRET-EKAREV-ERK1/2 transfection in MCF10A cells.

Generation of lentiviral and retroviral particles

Packaging of lentiviruses or retroviruses was performed following standard protocols. Viral supernatants were collected and filtered through 0.45 μm filters. Cells were subjected to four cycles of infection and selected using the appropriate antibiotic: neomycin for pSLIK-neo vector (150

720 μg/ml), hygromycin for pSLIK-hygro vector (100 μg/ml) or puromycin for EGFP-LifeAct or pBABE
721 vectors (2 μg/ml). After several passages, stable bulk populations were selected and induced by
722 Doxycycline Hyclate (2.5 μg/ml) in order to test: i) induction efficiency by Western Blotting and
723 quantitative RT-PCR (qRT-PCR), and ii) the homogeneity of the cell pool by immunofluorescence
724 staining, as previously shown[56].
725
726 **RNA interference**
727 siRNAs (small interfering RNAs) delivery was achieved by mixing 1 nM of specific siRNAs with
728 Optimem and Lipofectamine RNAiMAX Transfection Reagent (Life Technologies). The first cycle
729 of interference (reverse transfection) was performed on cells in suspension. The day after, a second
730 cycle of interference (forward transfection) was performed on cells in adhesion. The following
731 siRNAs were used for knocking down specific genes. All sequences are 5' to 3'.
732 Dynamin2 (DNM2): 5'-GACATGATCCTGCAGTTCA-3' (Dharmacon)
733 Clathrin heavy chain (CLTC): 5'-UAAAUUUCCGGGCAAAGAGCCCCC-3' (Riboxx)
734 NCKAP1 (NAP1): 5'-CUCGAAAUCUCAUCACUGATT-3' (Silencer Select, Ambion)
735 WASF4 (WAVE2): 5'-AGACCCUUCAUACUUCUUUTT-3' (Silencer Select, Ambion)
736 Reticulon 3 (RTN3) (Smart pool, Dharmacon):
737 5'-CAAUAUGAGAAUUCAGCGA-3'
738 5'-GGAAAUUGUCUACGUGUCU-3'
739 5'-GGGAAUAUGCACUGGCGAG-3'
740 5'-AAGGAAAGGCUCCGCCAUU-3'
741 Reticulon 3 (RTN3): 5'-CCCUGAAACUCAUUAUUCGUCUCUU-3' (Stealth, Invitrogen)
742 Reticulon 4 (RTN4): 5'-CCAGCCUAUUCCUGCUGCUUUCAUU-3' (Stealth, Invitrogen)
743 For each RNA interference experiment, negative control was performed with the same amount of
744 scrambled siRNAs. Silencing efficiency was controlled by qRT-PCR.

745

746 **Quantitative RT-PCR analysis**

747 Quantitative RT-PCR analysis was performed as previously shown[56]. Total RNA was extracted using
748 RNeasy Mini kit (Qiagen) and quantified by NanoDrop to assess both concentration and quality of
749 the samples. Reverse transcription was performed using SuperScript VILO cDNA Synthesis kit from
750 Invitrogen. Gene expression was analyzed using TaqMan Gene expression Assay (Applied
751 Biosystems). 0.1 ng of cDNA was amplified, in triplicate, in a reaction volume of 25 µl with 10 pMol
752 of each gene- specific primer and the SYBR-green PCR MasterMix (Applied Biosystems). Real-time
753 PCR was performed on the 14 ABI/Prism 7700 Sequence Detector System (PerkinElmer/Applied
754 Biosystems), using a pre-PCR step of 10 min at 95°C, followed by 40 cycles of 15 s at 95°C and 60
755 s at 60°C. Specificity of the amplified products was confirmed by melting curve analysis
756 (Dissociation Curve TM; PerkinElmer/Applied Biosystems) and by 6% PAGE. Preparations with
757 RNA template without reverse transcription were used as negative controls. Samples were amplified
758 with primers for each gene (for details see the Q-PCR primer list below) and GAPDH as a
759 housekeeping gene. The Ct values were normalized to the GAPDH curve. PCR experiments were
760 performed in triplicate and standard deviations calculated and displayed as error bars. Primer assay
761 IDs were: GAPDH, Hs99999905_m1; RAB5A, Hs00702360_s1; RAB5B, Hs00161184_m1 and
762 RAB5C, Hs00428044_m1, Dynamin2 (DNM2) Hs00974698_m1, Clathrin heavy chain (CLTC)
763 Hs00964480_m1, NAP1 Hs00980236_m1, WAVE2 Hs00819075_gh, Reticulon3 (RTN3)
764 Hs01581965_m1, Reticulon4 (RTN4) Hs01103689_m1.

765

766 **Immunoblotting**

767 For protein extraction, cells, previously washed with cold PBS, were lysed in JS buffer supplemented
768 with proteases and phosphatases inhibitors [50 mM HEPES PH 7.5, 50 mM NaCl, 1% glycerol; 1%
769 Triton X-100, 1.5 mM $MgCl_2$. 5 mM EGTA plus protease inhibitor cocktail (Roche, Basel,

770 Switzerland), 1 mM DTT, 20 mM Na pyrophosphate pH 7.5, 50 mM NaF, 0.5 M Na-vanadate in
771 HEPES pH 7.5 to inhibit phosphatases]. Lysates were incubated on ice for 10 minutes and cleared by
772 centrifugation at 13,000 rpm for 30 min at 4°C. Protein concentration was quantified by Bradford
773 colorimetric protein assay. The same amount of protein lysates was loaded onto polyacrylamide gel
774 in 5X SDS sample buffer. Proteins were transferred onto Protran Nitrocellulose Transfer membrane
775 (Whatman), probed with the appropriate antibodies and visualized with ECL western blotting
776 detection reagents (GE Healthcare). Membrane blocking and incubation in primary or secondary
777 antibodies were performed for 1h in TBS/0.1% Tween/5% milk for antibodies recognizing the total
778 proteins or in TBS/0.1% Tween/5% BSA for antibodies recognizing phosphorylated proteins.
779 Uncropped gels of the main immunoblots are presented in Supplementary Figure 11 and 12.
780

781 **Immunohistochemistry on DCIS and IDC**

782 Sections from archival human breast cancer samples were collected from the archives of the Tumor
783 Immunology Laboratory of the Human Pathology Section, Department of Health Sciences,
784 University of Palermo, Italy.
785 Immunohistochemistry was performed using a polymer detection method (Novolink Polymer
786 Detection Systems Novocastra, Leica Biosystems, Newcastle, Product No: RE7280-K).
787 Tissue samples were fixed in 10% buffered formalin and embedded in paraffin. Four-micrometers-
788 thick tissue sections were dewaxed and rehydrated. The antigen unmasking technique was performed
789 using Novocastra Epitope Retrieval Solution pH6 citrate-based buffer in thermostatic water bath at
790 98°C for 30 minutes. Subsequently, the sections were brought to room temperature and washed in
791 PBS-Tween. After neutralization of the endogenous peroxidases with 3% H_2O_2 and protein blocking
792 by a specific protein block, the samples were incubated 1h with monoclonal rabbit anti-human
793 RAB5A [EPR5438] - ab109534 (dilution 1:100, Abcam). Staining was revealed by polymer detection
794 kit (Novocastra, Ltd) and AEC (3-Amino-9-Ethylcarbazole) substrate chromogen. The slides were

795 counterstained with Harris hematoxylin (Novocastra, Ltd). All the sections were analyzed under a
796 Zeiss Axio Scope A1 optical microscope (Zeiss, Germany) and microphotographs were collected
797 using an Axiocam 503 Color digital camera with the ZEN2 imaging software (blue edition) (Zeiss
798 Germany).
799 For quantitative analysis of RAB5A IHC, non-overlapping areas, each corresponding to a x400 high-
800 power microscopic field, were selected from digital slide scans obtained using an Aperio CS2 slide
801 scanner (Leica Microsystems). A total of 80 fields corresponding to DCIS fields, fields with in situ
802 and associated infiltrating foci, and overtly-infiltrative IDC fields were analysed. The percentage of
803 strong positive cells (+3 score) per field was determined using the Aperio ImageScope software and
804 the Positive Pixel Count v9 Algorithm (Leica Microsystems).
805
806 ***In situ* mRNA hybridization on DCIS and IDC**
807 *In situ* mRNA hybridization for *RAB5A* transcript was performed on four micrometers thick FFPE
808 sections relative to DCIS and IDC. The RNAscope 2.0 HD Reagent Kit (Advanced Cell Diagnostics,
809 Hayward, CA, USA) was adopted according to the manufacturer's instructions, using an ad-hoc-
810 designed *RAB5A*-specific probe (C1 Custom Probe-Hs-*RAB5A* (targeting 424-2098 of
811 NM_001292048.1).
812 All the slides were analyzed under a Zeiss Axio Scope A1 optical microscope (Zeiss, Germany) and
813 microphotographs were collected using an Axiocam 503 Color digital camera with the ZEN2 imaging
814 software (Zeiss Germany).
815
816 **Cell streaming and wound healing assays**
817 As previously shown[56], cells were seeded in 6-well plate ($1.5*10^6$ cells/well) in complete medium
818 and cultured until a uniform monolayer had formed. RAB5A expression was induced, were indicated,
819 16 hours before performing the experiment by adding fresh complete media supplemented with 2.5
820 μg/ml Doxycycline Hyclate to cells. Comparable cell confluence was tested by taking pictures by

821 differential interference contrast (DIC) imaging using a 10x objective and counting the number of
822 nuclei/field. In cell streaming assay, medium has been refreshed before starting imaging. In wound
823 healing assay, cells monolayer was scratched with a pipette tip and carefully washed with 1X PBS to
824 remove floating cells and create a cell-free wound area. The closure of the wound was monitored by
825 time-lapse. Olympus ScanR inverted microscope with 10x objective was used to take pictures every
826 5-10 minutes over a 24 hours period (as indicated in the figure legends). The assay was performed
827 using an environmental microscope incubator set to 37°C and 5% CO2 perfusion. After cell induction,
828 Doxycycline Hyclate was maintained in the media for the total duration of the time-lapse experiment.
829 The percentage of area covered by cells (area coverage %) overtime and wound front speed were
830 calculated by MatLab software. In chemical inhibitors experiments, the inhibitor was added together
831 with Doxycycline Hyclate in fresh media 1 h before starting imaging. For cell streaming assay
832 performed on interfered cells, cells were interfered in suspension (first cycle) and directly plated at
833 the desired concentration, following the same conditions already described in "RNA interference"
834 section.
835 For detection of cryptic lamellipodia, MCF10A cells stably expressing EGFP-LifeAct were mixed in
836 a 1:10 ratio with unlabelled cells and seeded in cell streaming assay, as described before. Cell
837 migration was monitored by time-lapse phase contrast and fluorescence microscopy, collecting
838 images at multiple stage positions in each time loop. Olympus ScanR inverted microscope with 20x
839 objective (+1.6x Optovar) or with a Leica AM TIRF MC mic with HCX PL APO 63X/1.47NA
840 objective and equipped with Andor iXon DU-8285_VP was used to take pictures every 90 seconds.
841 For protrusion velocity analysis, the morphodynamic quantification was performed using the ImageJ
842 plugin ADAP (automated detection and analysis of protrusion) [57].
843 Each assay was done 5 times and at least 25 cells/condition were counted in each experiment. Where
844 indicated, PD0325901 or SCH772984 was added 1 h before imaging.
845

FRET Analysis

Using a customised macro in ImageJ, FRET data were analysed using the ratiometric approach. CFP, YFP and FRET images were background subtracted, converted in 32bits and the smoothed YFP image were tresholded and used as a mask to highlight the vesicular-like structures of interest. On these areas the average FRET/CFP ratio was then calculated as described in Kardash E. et al. [58]

3D morphogenesis assay

MCF10A morphogenesis assay was per formed as already described[67]. Briefly, MCF10A cells were trypsinized and resuspended in MCF10A culture medium. Eight-well chamber slides (#80826 IBIDI) were coated with 40 µl/well of Growth Factor Reduced Matrigel Matrix Basement Membrane HC 10.2 mg/ml (#354263, Corning) or with 1:1 mixture of Matrigel HC 10.2 mg/ml and Type I Bovine Collagen 3 mg/ml (#5005 Advanced BioMatrix). Once the matrix is polymerized, $2.5*10^3$ cells were plated into each well on the top of the matrix layer in culture medium supplemented with 2% Matrigel HC 10.2 mg/ml and 5 ng/ml EGF. Complete acini morphogenesis was allowed by incubating the cells for 3 weeks and replacing assay media every four days.

On day 21 acini were treated with 2.5 µg/ml Doxycycline Hyclate to induce RAB5A expression. Cells were maintained under stimulation for 6 days, changing the medium every 2 days, before fixation with 4% paraformaldehyde (PFA) and stained with specific antibodies. When inhibitors were used, the media were refreshed every day.

3D spheroid kinematic assay

MCF10DCIS.com cells were plated on Ultra-Low attachment surface 6-well plate (#3471 CORNING) at a density of $5*10^3$ cells/well. Cells were grown in serum-free condition for 10 days by adding fresh culture media every 2 days. Then every single well of spheres were collected and resuspended in 150 µl of 6 mg/ml Collagen Type I (#35429 CORNING), diluted in culture media, 50

mM Hepes, 0,12 $NaHCO_3$ and 5 mM NaOH. The unpolymerized mix sphere/collagen was placed in Eight-well chamber slides and incubated at 37°C for o/n. The day after, before imaging, 2.5µg/ml Doxycycline Hyclate was added over the polymerized collagen mix to induce RAB5A expression. For collagen mechanical stress analysis, 20 µl of FluoSpheres™ Sulfate Microspheres, 0.2 µm (#F8848 ThermoFisher) were added to the unpolymerized mix sphere/collagen and the protocol was carried out following the same conditions previously described.

Ex Vivo DCIS tumor slice motility assay

All animal experiments were approved by the OPBA (Organisms for the well-being of the animal) of IFOM and Cogentech. All experiments complied with national guidelines and legislation for animal experimentation. All mice were bred and maintained under specific pathogen-free conditions in our animal facilities at Cogentech Consortium at the FIRC Institute of Molecular Oncology Foundation and at the European Institute of Oncology in Milan, under the authorization from the Italian Ministry of Health (Autorizzazione N° 604-2016).

For mammary fat pad tumor development in NSG mice MCF10DCIS.com cells were trypsin detached, washed twice, and resuspended in PBS to a final concentration $2*10^5$/13 µl. The cell suspension was then mixed with 5 µl growth factor–reduced Matrigel and 2 µl Trypan blue solution and maintained on ice until injection. Aseptic conditions under a laminar flow hood were used throughout the surgical procedure. Female NOD.Cg-PrkdcscidIl2rgtm1Wjl/SzJ (commonly known as the NOD SCID gamma; NSG) mice, 6–9 weeks old, were anesthetized with 375 mg/Kg Avertin, laid on their backs, and injected with a 20-µl cell suspension directly in the fourth mammary fad pad. After 4 weeks mice were sacrificed and the primary tumors were removed, cut by a scalpel and each tumor slide was placed over a metal grid inserted in 6-well plate to allow tumors to grow on an interface air/culture medium. Before imaging, 2.5µg/ml Doxycycline Hyclate was added to tumor

slices culture media to induce RAB5A expression. Tumor cells were maintained under stimulation for 3 days, changing the medium every day.

Immunofluorescence

As previously shown[56], cells were fixed in 4% paraformaldehyde (PFA) and permeabilized with 0.1% Triton X-100 and 1% BSA 10 minutes (except for EEA-1 staining, permeabilized with 0.02% Saponin and 1% BSA 10 minutes and pERK1/2 staining, permeabilized with ice cold 100% Methanol for 10 minutes). In EGFR staining experiments, permeabilization step was avoided where indicated (non-permeabilized conditions) in order to detect only total cell surface EGFR. After 1X PBS wash, primary antibodies were added for 1 hour at room temperature. Coverslips were washed in 1X PBS before secondary antibody incubation 1 hour at room temperature, protected from light. FITC- or TRITC-phalloidin was added in the secondary antibody step, where applicable. After removal of not specifically bound antibodies by 1X PBS washing, nuclei were stained with 0.5 ng/ml DAPI. Samples were post-fixed and mounted on glass slides in anti-fade mounting medium (Mowiol). Antibodies were diluted in 1X PBS and 1% BSA. Images were acquired by wide-field fluorescence microscope or confocal microscope, as indicated in figure legends.

Immunofluorescence on MCF10A-derived acini was performed by fixing acini with 4% paraformaldehyde for 20 minutes at RT. Then cells were permeabilized with 0.5% TRITON X-100 in PBS for 10 minutes at 4ºC and incubated with blocking solution (PBS + 0.1% BSA + 10% goat serum) for 1 hour at RT. Acini were incubated with indicated primary antibodies diluted in blocking solution for o/n at 4ºC. The day after acini were incubated with indicated secondary antibodies diluted in blocking solution for 1 hour at RT. Finally, acini were incubated with DAPI in PBS for 20 minutes at RT. Samples were then maintained at 4ºC in PBS before imaging.

E-cadherin staining was analysed by confocal microscopy and images were processed to obtain the straightness index of the junction. “Junction length” was measured by tracking a straight line and

920 "junction tracking" was obtained by tracking manually the same junction following its profile. The
921 straightness index of the junction has been quantified as the ratio of the junction length and the
922 junction tracking.
923
924 **^{125}I-EGF internalization assay**
925 Internalization of ^{125}I-EGF was performed at low EGF (1 ng/ml) or high EGF (30 ng/ml) as described
926 in ref.[59].
927 Briefly, MCF10A cells were plated in 24-well plates in at least duplicate for each time point, plus
928 one well to assess non-specific binding. Cell monolayers were EGF-starved 24 hours and induced
929 overnight by Doxycycline Hyclate. The day after cells were incubated in assay medium (DMEM/F12
930 supplemented with Cholera Toxin (100 ng/ml), 0,1% BSA, 20mM Hepes, DOX (2.5µg/ml) and then
931 incubated at 37°C in the presence of 1 ng/ml ^{125}I-EGF, or 30 ng/ml EGF (1 ng/ml ^{125}I-EGF (Perkin
932 Elmer) + 29 ng/ml cold EGF. At different time points (2, 4, 6 min) the amount of bound ^{125}I-EGF
933 was measured with an acid wash solution pH 2.5 (0.2 M acetic acid, 0.5 M NaCl). Cells were then
934 lysed with 1N NaOH, which represents the amount of internalized ^{125}I-EGF. Non-specific binding
935 was measured at each time point in the presence of an excess of non-radioactive EGF (300 times).
936 After being corrected for non-specific binding, the rate of internalisation was calculated as the ratio
937 between internalised and surface-bound radioactivity. Surface EGFRs were measured by ^{125}I-EGF
938 saturation binding as described[60].
939
940 **EGF recycling assay**
941 Recycling assays of ^{125}I-EGF were performed as described in[60]. In brief, cell monolayers were EGF-
942 starved 24 hours and induced overnight by Doxycycline Hyclate. The day after cells were incubated
943 in assay medium (DMEM/F12 supplemented with Cholera Toxin (100ng/ml) , 0,1% BSA, 20mM
944 Hepes, DOX (2.5µg/ml), then incubated with ^{125}I-EGF (30 ng/ml: 5 ng/ml of ^{125}I-EGF + 25 ng/ml of

cold EGF) for 15 min at 37 °C, followed by mild acid/salt treatment (buffer at pH 4.5, 0.2 M Na acetate pH 4.5, 0.5 M NaCl) to remove bound EGF. Cells were then chased at 37°C in a medium containing 4 μg/ml EGF for the indicated times, to allow internalization and recycling. At the end of each chase time, the medium was collected, half was counted directly (free) and half was subjected to TCA precipitation to determine the amount of intact/recycled (TCA precipitable) and degraded (TCA soluble) ^{125}I-EGF present in it. Surface-bound ^{125}I-EGF was extracted by acid treatment (0.5M NaCl, 0.2M acid acetic). Finally, cells were lysed in 1N NaOH to determine intracellular ^{125}I-EGF. Data are expressed as the fraction of intact ^{125}I-EGF in the medium with respect to the total (total medium + total surface + total intracellular). Non-specific counts were measured for each time point in the presence of a 300-fold excess of cold ligand, and were never >3-10 % of the total counts.

Image acquisition

Time-lapse imaging of 3D acini/spheroids motility was performed on a Leica TCS SP8 laser confocal scanner mounted on a Leica DMi8 microscope equipped with motorized stage; a HC PL FLUOTAR 20X/0.5NA dry objective was used. A white light laser was used as illumination source. Leica Application Suite X (LAS X, https://www.leica-microsystems.com/products/microscope-software/details/product/leica-las-x-ls/) was the software used for all the acquisitions.

Image acquisition conditions were set to remove channel crosstalk, optimizing spectral detection bands and scanning modalities. ImageJ software was used for data analysis.

Collagen SHG analysis on collagen embedded MCF10DCIS spheroids was performed with a confocal microscope (Leica; TCS SP5) on an upright microscope (DM6000 CFS) equipped with blue (argon, 488 nm), yellow (561 nm solid state laser), and red (633 nm solid state laser) excitation laser lines with an HCX PL APO 40X/1.25-0.75NA oil immersion objective and controlled by Leica LAS AF Lite software (Leica). We used a two-photon excitation (2PE) technique with a pulsed infrared laser (Chameleon Ultra II; Coherent) at 980 nm.

EKAREV FRET analysis was performed using a DeltaVision Elite imaging system (Applied Precision) controlled by softWoRx Explorer 2.0 (Applied Precision) equipped with a DV Elite CMOS camera and an inverted microscope (IX71; Olympus) using a PlanApo N 60X/1.42NA oil-immersion objective lens.

Ex vivo DCIS tumor slice motility assay was performed using an Olympus IX83 inverted microscope controlled by The Olympus cellSens Standard software (Olympus, https://www.olympus-lifescience.com/en/software/cellsens/) and equipped with an iXon Ultra Andor (EMCCD) 16 bit camera using a UplanSApo 10X/0.4NA dry objective.

AFM measurements of collagen gel

Collagen gel samples at different concentration (2, 4, 6 mg/ml) were prepared as previously described in wells obtained by binding a microfabricated PDMS ring (height=2 mm, outer diameter=10 mm, inner diameter= 6 mm) to 24 mm-round glass coverslip via plasma treatment of the surfaces.

The stiffness of collagen gel samples was measured at 37°C by using NanoWizard3 AFM (JPK, Germany) coupled to an Olympus inverted microscope. A silicon nitride AFM probe (nominal spring constant of 0.03 N/m: NovaScan, USA) functionalized with a borosilicate microsphere (10 μm in diameter) was used for AFM indentation. Prior to the measurements, the deflection sensitivity and spring constant of the cantilever were calibrated in PBS on glass at 37°C.

Collagen gel stiffness was measured by bringing the bead-functionalized cantilever tip into contact with the matrix surface at 30 (or more) different positions. For each position five force curves were recorded. The contact force was set at a threshold value of 2 nN, the approach–retraction distance was 10 μm, and the approach velocity was 10 μm/s.

The data points below 0.8 μm indentation depth were used to calculate the elastic (Young's) modulus, by fitting the curves with the Hertz model:

$$F = \frac{4}{3}\frac{E}{(1-\nu^2)}\sqrt{R\delta^3} \qquad (1)$$

where F is the indentation force, E is the Young's modulus to be determined, ν is the Poisson's ratio, R is the radius of the spherical bead, and δ is the indentation depth.

Electron Microscopy

Electron microscopic examination was performed as previously described[61, 62]. A description of each process is described below.

Embedding: the tissue and 3D spheroids were fixed with of 4% paraformaldehyde and 2.5% glutaraldehyde (EMS, USA) mixture in 0.2 M sodium cacodylate pH 7.2 for 2 hours at RT, followed by 6 washes in 0.2 sodium cacodylate pH 7.2 at RT. Then cells were incubated in 1:1 mixture of 2% osmium tetraoxide and 3% potassium ferrocyanide for 1 hour at RT followed by 6 times rinsing in 0.2 M cacodylate buffer. Then the samples were sequentially treated with 0.3% thiocarbohydrazide in 0.2 M cacodylate buffer for 10 min and 1% OsO4 in 0.2 M cacodylate buffer (pH 6,9) for 30 min. Then, samples were rinsed with 0.1 M sodium cacodylate (pH 6.9) buffer until all traces of the yellow osmium fixative have been removed, washed in de-ionized water, treated with 1% uranyl acetate in water for 1 h and washed in water again (Mironov et al., 2004; Beznoussenko et al., 2015). The samples were subsequently subjected to de-hydration in ethanol and then in acetone and embedded in Epoxy resin at RT and polymerized for at least 72 h in a 60 °C oven. Embedded samples were then sectioned with diamond knife (Diatome, Switzerland) using Leica ultramicrotome (Leica EM UC7; Leica Microsystems, Vienna). Sections were analyzed with a Tecnai 20 High Voltage EM (FEI, Thermo Fisher Scientific, Eindhoven, The Netherlands) operating at 200 kV[62].

Measurement of the cellular velocities and trajectories on monolayers

Coarse-grained maps of the instantaneous cellular velocities were obtained by analysing time-lapse phase-contrast movies with a custom PIV software written in MATLAB[56]. The time interval between

consecutive frames was 5 min or 10 min. The interrogation window was 32X32 pixels (pixel size 1.29 μm or 1.6 μm), with an overlap of 50% between adjacent windows. The number of cells comprised within one field-of-view (FOV) was typically 2500. For a given monolayer, time-lapse images from different (typically from 5 to 10) FOVs were simultaneously collected.

The instantaneous root mean square velocity $v_{RMS}(t)$ of a cell monolayer was computed as $v_{RMS}(t) = \sqrt{\langle|\boldsymbol{v}(t)|^2\rangle_{\boldsymbol{x},j}}$, where $\boldsymbol{v}(t)$ is the instantaneous velocity vector and $\langle\cdot\rangle_{\boldsymbol{x},j}$ indicates an average over all grid points $\boldsymbol{x}$ (corresponding to the centers of the PIV interrogation windows) and FOVs j, respectively.

The instantaneous order parameter $\psi(t)$ of a cell monolayer was computed as $\psi(t) = \left\langle \frac{|\langle \boldsymbol{v}(t)\rangle_{\boldsymbol{x}}|^2}{\langle|\boldsymbol{v}(t)|^2\rangle_{\boldsymbol{x}}} \right\rangle_j$. This definition is such that $0 \leq \psi(t) \leq 1$. In particular, $\psi(t) = 1$ only if, within each FOV, the velocity field is perfectly uniform, *i.e.* all the cells in the monolayer move with the same speed and in the same direction. On the contrary $\psi(t) \cong 0$ is expected for a randomly oriented velocity field.

The vectorial velocity correlation functions were calculated as $C_{VV}(r) = \left\langle \frac{|\langle \boldsymbol{v}(\boldsymbol{x}+\boldsymbol{r},t)\cdot\boldsymbol{v}(\boldsymbol{x},t)\rangle_{\boldsymbol{x},t}|^2}{\langle|\boldsymbol{v}|^2\rangle_{\boldsymbol{x},t}} \right\rangle_j$. Unless otherwise stated in the main text, the temporal average $\langle\cdot\rangle_t$ was always performed over the time window comprised between 4 and 12 hours from the beginning of the image acquisition.

The velocity correlation function L_{corr} is obtained by fitting $C_{VV}(r)$ with a stretched exponential function of the form $f(r) = (1-\alpha)e^{-(r/L_{corr})^{\gamma}} + \alpha$. Here γ is a stretching exponent and α is an offset which is non-zero in presence of a collective migration of the monolayer.

Cellular trajectories $\boldsymbol{r}_m(t)$ were calculated by numerical integration of the instantaneous velocity field as obtained from the PIV analysis (see ref.[63] and reference therein). For each FOV a number of trajectories roughly corresponding to the number of cells was computed.

Mean squared displacements (MSDs) of the cells were calculated as $MSD(\Delta t) = \langle|\boldsymbol{r}_m(t+\Delta t) - \boldsymbol{r}_m(t)|^2\rangle$, where the average was performed over all the trajectories and, unless otherwise stated in the main text, in the time window comprised between 4 and 12 hours after the beginning of the

experiment. In order to estimate the persistence length L_{pers} of the cellular motion the MSD curves were fitted with a function of the form $g(\Delta t) = (u_0 \Delta t)^2 \left[1 + \left(u_0 \Delta t / L_{pers}\right)\right]^{-1}$. This expression describes a transition between a short-time ballistic-like scaling and a long-time diffusive scaling. The transition between the two regimes takes place for $\Delta t \approx 1/u_0 L_{pers}$, i.e. after the cell has travelled with an approximately constant velocity over a distance $\approx L_{pers}$.

Measurement of the cellular velocities of acini

Sequences of confocal Z stacks of 3D acini were analysed with an adapted PIV scheme in order to extract a representative value for the migration velocity, to assess the collective nature of the cellular motion and to detect the presence of a coherent rotational motion. Details about the imaging are given in the paragraph "Image acquisition".

The geometrical centre $\boldsymbol{x}_c$ of each acinus was determined as the centroid of the corresponding 3D fluorescent intensity distribution (Z stack) $I(\boldsymbol{x}|t)$: $\boldsymbol{x}_c = \frac{\sum I(\boldsymbol{x}|t)\boldsymbol{x}}{\sum I(\boldsymbol{x},t)}$, where the sum is performed over all voxels and time points. For each time point, the 3D fluorescent intensity distribution was radially projected onto the unit sphere centred in $\boldsymbol{x}_c$ leading to a sequence of 2D intensity maps $i(\theta, \varphi|t)$, where θ and φ are the polar and the azimuthal angle spanning the sphere, respectively. In practice, $i(\theta, \varphi|t)$ was obtained from a representation of $I(\boldsymbol{x}|t)$ in spherical coordinates, after summation over the radial coordinate. For each time point, i is represented by a 512x128 matrix, each element covering the Cartesian product of angular intervals of constant amplitudes $\Delta\,\theta = \pi/512$ and $\Delta\,\varphi = 2\pi/128$, respectively.

We performed on i a 2D PIV analysis as described in the previous paragraph, by treating (θ, φ) as Cartesian coordinates. The obtained coarse-grained velocity fields $[u_\theta(\theta, \varphi|t), u_\varphi(\theta, \varphi|t)]$ (in units of rad/hr) were then used to reconstruct the tangential velocity field $\boldsymbol{v}(\theta, \varphi) = R_0 \left(u_\theta(\theta, \varphi|t)\boldsymbol{n}_\theta +\right.$

$u_\varphi(\theta,\varphi|t)\sin\theta\,\boldsymbol{n}_\varphi\big)$ of the acinus. Here, $\boldsymbol{n}_\theta$ and $\boldsymbol{n}_\varphi$ are the polar and the azimuthal unit vector, respectively and $R_0=\sqrt{\frac{\sum I(\boldsymbol{x}|t)(\boldsymbol{x}-\boldsymbol{x_c})^2}{\sum I(\boldsymbol{x},t)}}$ is the radius of gyration of the acinus.

The root mean squared velocity was calculated as $v_{RMS}(t)=\sqrt{\langle|\boldsymbol{v}|^2\rangle}$, where the angular brackets indicate an average performed over the whole sphere. The presence of a pattern of global rotation was monitored by measuring the total angular momentum $\boldsymbol{l}=\langle\boldsymbol{r}\times\boldsymbol{v}\rangle$, where $\boldsymbol{r}$ is a unit vector spanning the whole sphere. The direction of $\boldsymbol{l}$ identifies the orientation of the axis of instantaneous rotation. The collective nature of the cellular motility is captured by the non-dimensional rotational order parameter $\psi=\frac{\pi}{2}\frac{|\boldsymbol{l}|^2}{v_{RMS}^2}$. The normalization of the order parameter is such that, for a rigidly rotating sphere, $\psi=1$, while, in the absence of coordinated motion one expects $\psi\cong 0$.

Phase contrast Rotation analysis of acini: Maps of the instantaneous cellular velocities were obtained by analysing time-lapse movies and performing a PIV (Particle Image Velocimetry) analysis using the Matlab MPIV toolbox (http://www.oceanwave.jp/softwares/mpiv/ and https://www.mathworks.com/help/matlab/ref/curl.html) with the MQD (Minimum Quadric Differences) algorithm and an interrogation window of 24 pixels X 24 pixels with an overlap of 50%. From the maps of the instantaneous cellular velocities for each frame, we computed the map of curl of the velocity field using the Matlab function *curl*. For each frame, we evaluated the rotation of the acini as the average of absolute value of the curl map.

Kinematic and dynamical analysis of spheroids

Overall motility and internal dynamics of control and RAB5A-MCF10A-expressing mCherry-H2B spheroids were measured by analysing time sequences of confocal Z stacks, according to the following procedure, implemented in a custom MATLAB® code. More details about the imaging can be found in the paragraph “Image acquisition”.

We indicate with $R(\boldsymbol{\Theta}, \boldsymbol{U})$ the roto-translational operator given by the composition of a 3D rotation by an angle $|\boldsymbol{\Theta}|$ around the axis identified by the direction of the 3D vector $\boldsymbol{\Theta}$ and a translation of vector $\boldsymbol{U}$. $R(\boldsymbol{\Theta}, \boldsymbol{U})$ is a linear operator and its numerical implementation as a transformation between 3D matrices (Z stacks) was realized *via* the MATLAB functions *imwrap* and *affine3d*.

Let us consider two 3D stacks $I(\boldsymbol{x}, t)$ and $I(\boldsymbol{x}, t + \Delta t_0)$, where Δt_0 is delay between consecutive stacks. We define $\boldsymbol{\Omega}(t)$ and $\boldsymbol{U}(t)$ as the 3D vectors that minimize the distance d (namely, the variance of the difference) between $I(\boldsymbol{x}, t + \Delta t_0)$ and $R(\boldsymbol{\omega}\Delta t_0, \boldsymbol{u})I(\boldsymbol{x}, t)$: $d(\boldsymbol{\omega}, \boldsymbol{u}|t) = \|I(\boldsymbol{x}, t + \Delta t_0) - R(\boldsymbol{\omega}\Delta t_0, \boldsymbol{u})I(\boldsymbol{x}, t)\|^2$. Numerically, the minimization is performed by exploiting the MATLAB function *imregtform*. In substance, .

The residual internal restructuring dynamics is measured *via* a general $R\left(\boldsymbol{\Omega}(t)\Delta t_0, \boldsymbol{U}(t)\right)$ is the rigid transformation that reproduces at best the changes occurred in $I(\boldsymbol{x}, t)$ during the time interval Δt_0. According to the definitions above, $\boldsymbol{\Omega}(t)$ provides the best estimate for the instantaneous vectorial angular velocity of the spheroid, the direction of $\boldsymbol{n}(t) = \frac{\boldsymbol{\Omega}(t)}{|\boldsymbol{\Omega}(t)|}$ identifying the axis of instantaneous rotation. The temporal persistence of the rotational motion is captured by the orientational correlation function $C_{\boldsymbol{n}}(\Delta t) = \langle \boldsymbol{n}(t + \Delta t) \cdot \boldsymbol{n}(t) \rangle_t$, where $\Delta t = n\Delta t_0$. In order to estimate the rotational correlation time τ_P, $C_{\boldsymbol{n}}(\Delta t)$ was fitted with an exponential function of the form $f(\Delta t) = \exp(-\Delta t/\tau_P)$ization to the 3D case of a recently introduced method (Difference Variance Analysis, DVA) for the quantification of the dynamics of particulate soft matter systems[64]. The non-rigid part of the changes occurring within a spheroid between time t and $t + \Delta t$, where $\Delta t = n\Delta t_0$, is captured by the parameter: $q(\Delta t, t) = 1 - \beta^{-1}\|I(\boldsymbol{x}, t + \Delta t) - T(\Delta t, t)I(\boldsymbol{x}, t)\|^2$, where $T(\Delta t, t) = R(\boldsymbol{\Omega}(t + n\Delta t_0)\Delta t, \boldsymbol{U}(t + n\Delta t_0)) \circ R(\boldsymbol{\Omega}(t + (n-1)\Delta t_0)\Delta t, \boldsymbol{U}(t + (n-1)\Delta t_0)) \circ \ldots \circ R(\boldsymbol{\Omega}(\mathrm{t})\Delta t, \boldsymbol{U}(t))$ is the composition of elementary roto-translations and $\beta = 2\left(\langle I^2 \rangle_{t,\boldsymbol{x}} - \langle I \rangle_{t,\boldsymbol{x}}{}^2\right)$. The definition of q is such that, neglecting noise and truncation errors, $q \cong 1$ if the spheroids is immobile or if it undergoes a perfectly rigid displacement and/or rotation, with no relative motion between different cells. On the

contrary, one gets $q \cong 0$ when almost all the cells have performed positional rearrangements on a length scale comparable with their size, leading to a substantial change in the local structure[64]. We consider the so-called overlap parameter Q, obtained as a temporal average of q: $Q(\Delta t) = \langle q(\Delta t, t)\rangle_t$.

By fitting the decay of Q with an exponential function $Q(\Delta t) = Q_0 e^{-\Delta t/\tau}$, we can extract an estimate of the characteristic correlation time τ after which an almost complete change in the cellular configuration has occurred.

Moreover, in order to spot potential spatial inhomogeneities in the dynamics, in particular a dependence of the relaxation time on the radial coordinate $r = |\boldsymbol{x}|$ (in a reference frame where $\boldsymbol{x} = 0$ corresponds to the center of the spheroid), we also considered a space-resolved version $Q_s(\Delta t, r) = \langle q_s(\Delta t, t, \boldsymbol{x})\rangle_{t,|\boldsymbol{x}|=r}$ of the above-defined overlap parameter, where $q_s(\Delta t, t, \boldsymbol{x}) = 1 - {\beta_s}^{-1}[I(\boldsymbol{x}, t + \Delta t) - T(\Delta t, t)I(\boldsymbol{x}, t)]^2$ and $\beta_s = 2\left(\langle I^2\rangle_{t,|\boldsymbol{x}|=r} - \langle I\rangle_{t,|\boldsymbol{x}|=r}{}^2\right)$. According to the above definitions, the decay of $Q_s(\Delta t, r)$ captures the relaxation dynamics at different distances r from the center of the spheroid. Instead of performing a fit, we extracted the relaxation rate $\Gamma(r) = 1/\tau(r)$ associated with the decay of $Q_s(\Delta t, r)$ as a function the delay time Δt in a simple and robust manner by considering the difference quotient at the origin of the temporal axis: $\Gamma(r) \cong -[Q_s(\Delta t_0, r) - Q_s(0, r)]/\Delta t_0$.

Reference-free estimation of the fluctuating Root Mean Square stresses: Stress Fluctuation Microscopy

Spatial maps of the Root Mean Square (RMS) stresses in the ECM surrounding MCF10.DCIS.com spheroids were obtained by analyzing the positional fluctuations of embedded, fluorescent tracer particles by using Stress Fluctuation Microscopy, as described below. The procedure was applied to 4D stacks ($xyzt$) obtained from time-lapse confocal acquisitions. Each stack included 72 time points and 35 Z planes, each plane having a resolution of 512x512 pixels. Delay between frames was 20 minutes, voxel size was (xyz) 0.57x0.57x3.00 μm^3.

The instantaneous velocity field $\boldsymbol{v}(\boldsymbol{x},t) = \partial_t \boldsymbol{u}(\boldsymbol{x},t)$ associated with the motion of the fluorescent tracers embedded in the ECM was obtained *via* a custom Lucas-Kanade optical flow algorithm [65] implemented in MATLAB (Gaussian weighted window (σ = 2 pixels), mesh size: 10 pixels) (Supplementary Figure 10A-B and Supplementary Movie 27). Here, $\boldsymbol{u}(\boldsymbol{x},t)$ represents the displacement field of the ECM with respect to its (unknown) mechanical equilibrium condition. We note that the time derivative of the strain tensor $\varepsilon_{ij}(\boldsymbol{x},t) \equiv \partial_i u_j(\boldsymbol{x},t)$ can be written in terms of a spatial derivative of the velocity as $\partial_t \varepsilon_{ij}(\boldsymbol{x},t) = \partial_i v_j(\boldsymbol{x},t)$. This last equality enables estimating the mean squared value (MSV) of the strain fluctuation $\Delta\varepsilon_{ij}(\tau) \equiv \varepsilon_{ij}(t_0+\tau) - \varepsilon_{ij}(t_0)$ as an integral of the temporal correlation function $C_{ij}(t) \equiv \langle \partial_i v_j(t+t_0) \partial_i v_j(t_0) \rangle$ [66]

$$\langle \Delta\varepsilon_{ij}(\tau)^2 \rangle = 2 \int_0^\tau (\tau - |t|)\, C_{ij}(t) dt, \qquad (2)$$

where the dependence on the spatial coordinate $\boldsymbol{x}$ has been omitted for clarity. Temporal correlation functions $C_{ij}(t)$ evaluated in proximity of the boundary of different spheroids are shown in Supplementary Fig. 10C. We found that $\langle \Delta\varepsilon_{ij}(\tau)^2 \rangle$ rapidly saturates to a τ-independent asymptotic value $\langle \Delta\varepsilon_{ij}{}^2 \rangle$. Once obtained the MSV $\langle \Delta\varepsilon_{ij}{}^2 \rangle$ of the strain fluctuation, the MSV $\langle \Delta\sigma_{ij}{}^2 \rangle$ of the *stress* fluctuation can be obtained *via* the constitutive equations of the material, which we assumed to be isotropic and homogeneous. This assumption relies on the fact that the length scales probed in our experiments (a few microns) are about one order of magnitude larger than the characteristic mesh size on the collagen network [67]. Moreover, we adopt the approximation of negligible compressibility (*i.e.* that the Poisson ratio of the material is 0.5) [68]. Under these hypotheses, the mechanical response of the material is described in terms of a single parameter, namely the Young modulus E, that we measured directly with AFM indentation experiments.

In this work, the above-described procedure has been applied on the equatorial plane of each spheroid, by considering the 2D intensity distribution obtained as a z-average of 3 adjacent confocal planes.

Therefore, only the in-plane components of the velocity, strain and stress were considered. In this simplified geometry, the diagonal components of the fluctuating stress tensor are given by

$$\langle \Delta\sigma_{11}{}^2 \rangle = \left(\frac{E}{1-\nu^2}\right)^2 \left(\langle \Delta\varepsilon_{11}{}^2 \rangle + \nu^2 \langle \Delta\varepsilon_{22}{}^2 \rangle\right) \quad (3)$$

$$\langle \Delta\sigma_{22}{}^2 \rangle = \left(\frac{E}{1-\nu^2}\right)^2 \left(\langle \Delta\varepsilon_{22}{}^2 \rangle + \nu^2 \langle \Delta\varepsilon_{11}{}^2 \rangle\right) \quad (4)$$

while the mean value of the normal stress can be calculated as

$$\langle \Delta\sigma^2 \rangle = E^2 \frac{(1+\nu^2)}{(1-\nu^2)^2} \langle \Delta\varepsilon^2 \rangle \quad (5)$$

where $\langle \Delta\varepsilon^2 \rangle = (\langle \Delta\varepsilon_{11}{}^2 \rangle + \langle \Delta\varepsilon_{22}{}^2 \rangle)/2$. The level of uncertainty associated with this analysis was estimated by applying the described procedure to n=5 confocal stacks collected with the same acquisition parameters in portions of the fluorescent particles-seeded collagen gel far from the embedded spheroids. The obtained MSV of the "background" normal stress was $\langle \Delta\sigma^2 \rangle|_{bgd} = 50 \pm 3\ Pa^2$, about one order of magnitude smaller of the peak values obtained in the presence of a spheroid (see Supplementary Figure 10D). We estimated the Root Mean Square (RMS) value σ_{RMS} of the fluctuating stress in the presence of the spheroids by subtracting this spurious contribution from the measured MSV: $\sigma_{RMS} = \sqrt{\langle \Delta\sigma^2 \rangle - \langle \Delta\sigma^2 \rangle|_{bgd}}$. We note that, in principle, the above-described formalism could be easily adapted to reconstruct the full 3D distribution of the fluctuating stresses. Nevertheless, the limited axial resolution of the confocal acquisition system imposes a substantial limitation on the accuracy of the reconstructed tracer's displacements along z, with an obvious impact on the reconstructed stresses. The solution of this problem is beyond the scope of this work and will be investigated in future publication.

Statistical analysis

Student's unpaired and paired t-test was used for determining the statistical significance whenever we compared in a pairwise fashion two distinct distribution. In the case of the endosome size distribution comparing multiple treatments (Control, RAB5A, RAB5B and RAB5C) Chi-sqaure or Mann-

Whitney or Tuckey tests were applied as indicated. In Figure 8C, P-values of the Kaplan Mayer curves are were calculated using a log-rank test. Significance was defined as $*p < 0.05$; $**p < 0.01$; $***p < 0.001$ and $****p < 0.0001$. Statistic calculations were performed with GraphPad Prism 8 Software (https://www.graphpad.com/scientific-software/prism/). Data are expressed as mean ± SD, unless otherwise indicated.

References (Methods)

53. Komatsu, N. *et al.* Development of an optimized backbone of FRET biosensors for kinases and GTPases. *Mol Biol Cell* **22**, 4647-4656 (2011).
54. Innocenti, M. *et al.* Abi1 regulates the activity of N-WASP and WAVE in distinct actin-based processes. *Nat Cell Biol* **7**, 969-976 (2005).
55. Stradal, T.E. *et al.* Regulation of actin dynamics by WASP and WAVE family proteins. *Trends Cell Biol* **14**, 303-311 (2004).
56. Malinverno, C. *et al.* Endocytic reawakening of motility in jammed epithelia. *Nature materials* **16**, 587-596 (2017).
57. Barry, D.J., Durkin, C.H., Abella, J.V. & Way, M. Open source software for quantification of cell migration, protrusions, and fluorescence intensities. *J Cell Biol* **209**, 163-180 (2015).
58. Kardash, E., Bandemer, J. & Raz, E. Imaging protein activity in live embryos using fluorescence resonance energy transfer biosensors. *Nat Protoc* **6**, 1835-1846 (2011).
59. Caldieri, G. *et al.* Reticulon 3-dependent ER-PM contact sites control EGFR nonclathrin endocytosis. *Science* **356**, 617-624 (2017).
60. Sigismund, S. *et al.* Clathrin-mediated internalization is essential for sustained EGFR signaling but dispensable for degradation. *Dev Cell* **15**, 209-219 (2008).
61. Beznoussenko, G.V., Ragnini-Wilson, A., Wilson, C. & Mironov, A.A. Three-dimensional and immune electron microscopic analysis of the secretory pathway in Saccharomyces cerevisiae. *Histochem Cell Biol* **146**, 515-527 (2016).
62. Beznoussenko, G.V. & Mironov, A.A. Correlative video-light-electron microscopy of mobile organelles. *Methods Mol Biol* **1270**, 321-346 (2015).
63. Park, J.A. *et al.* Unjamming and cell shape in the asthmatic airway epithelium. *Nature materials* **14**, 1040-1048 (2015).
64. Pastore, R., Pesce, G. & Caggioni, M. Differential Variance Analysis: a direct method to quantify and visualize dynamic heterogeneities. *Scientific reports* **7**, 43496 (2017).
65. Barron, J.L., Fleet, D.J. & Beauchemin, S.S. Performance of optical flow techniques. *Int. J. Comput. Vision* **12**, 43-77 (1994).
66. Kubo, R. The fluctuation-dissipation theorem. *Reports on Progress in Physics* **29**, 255-284 (1966).
67. Yang, Y.L., Leone, L.M. & Kaufman, L.J. Elastic moduli of collagen gels can be predicted from two-dimensional confocal microscopy. *Biophys J* **97**, 2051-2060 (2009).
68. Castro, A.P. *et al.* Combined numerical and experimental biomechanical characterization of soft collagen hydrogel substrate. *J Mater Sci Mater Med* **27**, 79 (2016).

1230
1231
1232
1233
1234